



Comprehensive corrosion evaluation of sintered Al/Ni-SiC composite by CuL2 nanocomplex as a green inhibitor in 1M HCl solution

Shimaa Abolkassem ¹, Lamiaa Z Mohamed ^{2*}, Shimaa Hosny ³, Omayma Ahmed El kady ⁴
Ayman Elsayed ¹, Ghalia A. Gaber ⁵



¹ Powder Technology Division, Manufacturing Technology Institute, Central Metallurgical Research and Development Institute, Helwan El-Tabbin, P.O. Box 87, Cairo, Egypt

² Mining, Petroleum, Metallurgical Engineering Dept., Faculty of Engineering, Cairo University

³ Chemistry Department, Faculty of Science, New Valley University, El-Kharga, 72511, Egypt

⁴ Powder Metallurgy Division, Manufacturing Department, Central Metallurgical R&D Institute, P.O.87 Helwan, 11421 Cairo, Egypt.

⁵ Faculty of science, chemistry department, Al Azhar University

Abstract

The corrosion performance of Al/Ni-SiC composites prepared by powder technology using both vacuum and hot compaction techniques for the sintering process is explored, highlighting the importance of their electrochemical and chemical properties. The research also examines the corrosive effects on aluminum metal matrix composites (AMMCs) and other solid wastes. Although AMMCs demonstrate strong mechanical and tribological properties, their corrosion resistance remains a challenge. The CuL2 nanocomplex (green nanocomplex) is prepared in a simple, rapid, and eco-friendly manner using coriandrum sativum extract in ethanol, which is employed to enhance the corrosion resistance of Al/Ni-SiC composites. Additionally, the corrosion behavior of Al/Ni-SiC composites with the CuL2 nanocomplex has been theoretically investigated using density functional theory. The investigation demonstrated that the samples with the lowest corrosion rate (CR) values were consolidated using hot compaction and vacuum mixing. The CR decreased with increasing concentrations (5%, 10%, and 15%) of nickel-coated SiC particles by weight. Specifically, the nickel-coated SiC particles in the hot compaction mix and vacuum mix at 15% in 1M HCl exhibited CR values of 1.17 mm/y and 0.39 mm/y, respectively.

Keywords: Al/Ni-SiC Composite, Synergistic CuL2 nanocomplex; Corrosion inhibition; Electrochemical Techniques; Density functional theory.

1. Introduction

In metal matrix composites (MMCs), one material acts as the matrix while the other serves as the reinforcement. During the manufacturing process, stress is transferred from the matrix material to the reinforcement materials, thereby providing mechanical strength in a specific direction to the composite. Ideally, a good MMC exhibits ductility in the matrix and brittleness in the reinforcement. MMCs excel over monolithic materials in several ways, including being lightweight, having excellent high-temperature characteristics, possessing a low coefficient of thermal expansion, and offering better abrasion resistance. Additionally, they display enhanced stiffness and strength compared to monolithic materials [1, 2]. As a result, MMCs are gradually replacing many traditional alloys in various sectors, including transportation, the marine industry, outdoor leisure, and military hardware [3].

Because of their low cost, high strength-to-weight ratio, ease of production, and widespread use, aluminum and its alloys have been the preferred structural materials for the automotive and aerospace industries [4, 5]. Nevertheless, due to their chemical composition, these alloys are prone to corrosion, which significantly shortens the lifespan of these structures. Therefore, improving the corrosion resistance of aluminum alloys is essential for their future applications [6, 7]. The promising future of aluminum-based metal matrix composites (AMMCs) as preferred materials for a wide range of technical applications has garnered significant interest. They boast exceptional mechanical properties, wear resistance, and corrosion resistance. Additionally, they are more cost-effective to produce compared to other metal matrix composites [8, 9]. Currently, AMMCs are reinforced with industrial by-products such as red mud and fly ash, as well as agro-based materials like bagasse and rice husk ash [10]. Despite their advantages, the presence of the reinforcing phase in AMMCs can make them susceptible to corrosion in certain situations. Compared to base metal, AMMCs generally exhibit lower corrosion resistance. This is

*Corresponding author e-mail: lamiaa.zaky@cu.edu.eg; (Lamiaa Z Mohamed).

Received date 15 August 2024; Revised date 06 October 2024; Accepted date 27 October 2024

DOI: 10.21608/ejchem.2024.312822.10207

©2025 National Information and Documentation Center (NIDOC)

because Al alloys are naturally resistant to corrosion and crack development due to the thick oxide layers that may be formed on their surfaces. However, in aluminum-based metal matrix composites, the reinforcing phase can disrupt this passive coating, increasing its vulnerability to corrosion.

Corrosion is a common and unavoidable issue that can cause significant damage and financial losses when metal structures are exposed to it. In various environments, including aquatic systems, one of the most broadly used metals in engineering and metallurgical structures is particularly affected [11]. Ceramic particles, for example, Al₂O₃, SiO₂, TiC, and WC exhibit high hardness and corrosion resistance. When these particles are present in the form of nanocrystals, they enhance the mechanical and corrosion resistance of the coatings [12, 13]. Silicon carbide nanoparticles are widely employed in coatings by researchers because of their excellent oxidation resistance, superior wear resistance, and corrosion resistance. Previous studies have shown that the addition of micro and/or nano SiC particles to the Al alloy metal matrix composite enhances its surface characteristics [4].

To safeguard metal surfaces from corrosive environments or alleviate their effects, corrosion inhibitors are employed. These inhibitors can be either natural or synthetic [14]. Industries such as food and pharmaceuticals can derive benefits from natural inhibitors due to their renewable nature, biodegradability, and safety for human use [15]. Synthetic inhibitors, on the other hand, are chemically synthesized to offer high effectiveness in specific corrosive conditions. Examples of synthetic inhibitors include amine salts, phosphates, and nitrites [16]. Synthetic inhibitors excel over their natural counterparts in terms of effectiveness, versatility, reliability, and storage stability [17]. Synthetic inhibitors facilitate the formation of a protective coating on metal surfaces, shielding them from corrosive substances. They are particularly effective in harsh and corrosive environments with high concentrations of contaminants, salts, and other pollutants [18]. Due to the challenges and costs associated with maintaining offshore platforms, pipelines, and nuclear power plants, these locations are ideal for the application of synthetic inhibitors. Based on their mechanism of action, synthetic inhibitors are categorized into three main types: anodic, cathodic, and mixed-type inhibitors. [19].

Schiff bases interact with metals to prevent corrosion in acidic environments, protecting Fe, Cu, Al, and Zn [20, 21, 22]. Our understanding of the fundamental mechanisms underlying molecule interactions with various materials and organic surfaces has been significantly advanced using density functional theory (DFT) and molecular dynamics (MD) simulations [23, 24, 25]. Performance can be optimized by designing corrosion inhibitors tailored for specific applications. Extensive research has focused on using DFT and MD for corrosion inhibition [26, 27, 28]. The electrophilicity index (ω) was introduced by Parr et al. [29], employing thermodynamic parameters to quantify the positive energy shift occurring as a chemical system approaches electron saturation. The movement of electrons from the highest occupied molecular orbital (HOMO) to the lowest unoccupied molecular orbital (LUMO) is indicated by this energy shift. The energy gap value significantly influences the adsorption of inhibitor molecules on metal surfaces. Narrowing this gap enhances both reactivity and inhibition efficiency [30, 31]. More energy is required to remove an electron from the HOMO, which improves inhibitor activity [32]. Molecules with high chemical activity but low kinetic stability, characterized by minimal energy gaps (Gap values), are referred to as "soft" [4]. Organic chemicals reduce corrosion by accepting free electrons and transferring them to empty orbitals in metal [33, 34, 35].

The literature has paid scant attention to the impact of Schiff base corrosion on Al composites produced via various powder metallurgy techniques. This study addresses corrosion prevention in Al/Ni-SiC composites, fabricated using diverse powder metallurgy methods, by introducing a novel Schiff base (CuL₂ nanocomplex). The composite, reinforced with SiC and Ni, was processed using vacuum and hot compaction procedures. The corrosion resistance of the Al/Ni-SiC composites in 1M HCl, enhanced by the CuL₂ nanocomplex (green inhibitor), was evaluated using gravimetric techniques, potentiodynamic polarization (PDP), and theoretical DFT methodologies. Additionally, scanning electron microscopy (SEM) and energy dispersive X-ray analysis (EDX) were employed to assess the morphology and elemental composition of before and after corrosion of the Al/Ni-SiC composite with different conditions.

2. Experimental work

Aluminum and silicon carbide powders with particle sizes ranging from 5-10 μm and 2-20 μm , respectively, were used, boasting purity levels of 98.9% and 99.98%. These components were sourced from Organik Kimya San. Co. of Turkey and Loba Chemie Pvt. Ltd. of India. The SiC particles were coated with 10 wt% nano-Ni through an electroless coating process.

Table 1 outlines the electroless coating procedure and its chemical bath composition. Sodium hypophosphite was used to reduce NiCl₂.6H₂O after adjusting the medium pH to 9 and the temperature to approximately 100°C [36, 37]. The nickel-coated SiC powder was then mixed with Al powder in 5, 10, and 15% weight ratios using a ball mill at a ball-to-powder ratio of 10:1 for 5 hours [38].

The powder mixtures were solidified using one of three procedures. In the first method, one set of specimens was sintered in a vacuum oven at 600°C for an hour after being cold compacted at 840 MPa using a uniaxial press. The heating cycle included two holding phases: one at 250°C to melt away the paraffin wax, and another at 600°C to complete the sintering process. The second method involved preparing the samples by pressing them at 840 MPa in a die heated to 550°C. After 30 minutes of heating, these samples were hot-pressed into high-density blocks.

Table 1. Electroless deposition reaction bath concentrations of different compounds

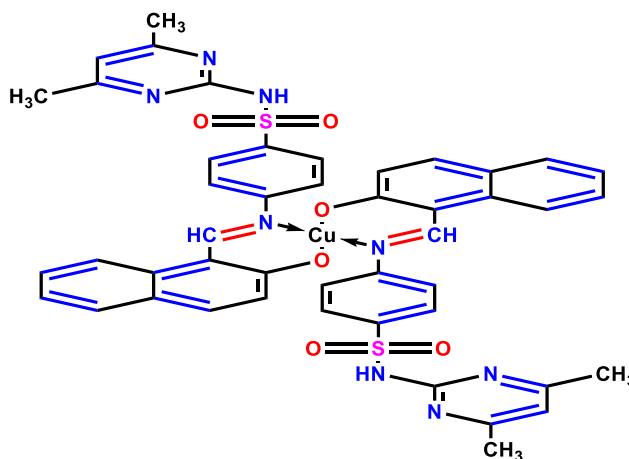
Compositions	Concentration g/l
Sodium hypophosphite	100
NiCl ₂ .6H ₂ O	100
Potassium sodium tartrate	80
NH ₄ Cl	50
pH	~9.2
Temperature	~92

2.1. Composite characterization

The densities of the sintered samples were determined using the Archimedes principle in a water bath, by weighing the samples both in air and in distilled water. The SEM equipped with EDX, they were used to analyze the microstructure, employing detection modes for both backscattered and secondary electrons. This technique enabled the examination of the powder particles' microstructure, size, and shape. The samples were prepared for microstructure observation through a series of steps: mounting, grinding with SiC grit sheets, and polishing with alumina paste with a particle size of 3 μm. The phase structure was analyzed using the X'pert PRO PANalytical model and X-ray diffraction (XRD) with Cu Kα radiation (λ=0.15406 nm). These experiments aimed to identify any new phases, such as Al, Ni, and SiC, that may have formed during sintering.

2.2. Green Synthesis of nano complex

As documented in our previous papers, the CuL₂ nanocomplex shown in Fig. 1 was synthesized using a medium with an ethanol/Coriandrum sativum (CS)/EtOH ratio of 1:1 [39, 40, 41].


Fig. 1. Structure of CuL₂ nanocomplex inhibitor

2.3. The corrosive substance

To prepare the 1M HCl medium, AR-grade 37% concentrated acid was diluted with bi-distilled water. The experiments were conducted in a 1M HCl solution, both with and without varying concentrations of CuL₂ nanocomplex (100–600 ppm).

2.4. Weight loss (WL) measurements

Initially, a digital scale was used to measure the weight of the samples. Subsequently, the samples were submerged in 100 mL of 1M HCl at 25°C for five days, with and without varying concentrations of the CuL₂ nanocomplex (100 ppm). A Model FA 2104A sensitive analytical balance (210 g capacity, 0.1 mg readability) was used to weigh the samples after they were dried in a moisture-free desiccator and removed from the test solution following the immersion period. The weight reduction was determined by the difference in weight before and after immersion. Corrosion rate (CR) values were calculated using Eq. (1) [42, 43]:

$$CR (mm/y) = \frac{\Delta W \times K}{A T D} \quad (1)$$

The CR in mm/y was determined. This calculation involved the constant K (8.76x10⁴), the exposure time (T), the area (A) in mm², the weight difference (ΔW) before and after immersion, and the density (D) in g/cm³ for the Al matrix. The degree of surface coverage (θ) was calculated using Eq. (2):

$$\theta = \frac{W_0 - W_i}{W_0} \quad (2)$$

Where W_i and W_0 represent the weight losses of the Al matrix in i with/without inhibitors, respectively. The inhibition efficiency (IE%) was calculated according to Eq. (3) [44]:

$$IE\% = \theta \times 100 \quad (3)$$

2.5. Potentiodynamic Polarization

The PDP technique was used to scan the electrode potential at 2 mVs^{-1} , varying the potential between -1.2 and $+0.5 \text{ V}$. The resulting PDP curves provided valuable insights into the material's corrosion behavior. The experiments were repeated for each inhibitor concentration. To ensure consistency, fresh electrolyte was prepared for each experiment, and the Al matrix was abraded before testing. Electrochemical experiments were conducted using the Electronic Potentiostat scan Wenking POS 73, and various electrochemical parameters were calculated, including corrosion potential (E_{corr}), corrosion current density (I_{corr}), CR, anodic Tafel slope (β_a), and cathodic Tafel slope (β_c). The inhibition efficiency, indicating the effectiveness of the inhibitor, was also determined using Eq. (4).

$$IE\% = \left[1 - \frac{I_{\text{corr}}}{I_{\text{corr}}^0} \right] \times 100 \quad (4)$$

Where, I_{corr}^0 and I_{corr} express the corrosion current densities in the absence and presence of an inhibitor, respectively. The value of $\left[1 - \frac{I_{\text{corr}}}{I_{\text{corr}}^0} \right]$ corresponds to the surface coverage, indicating the degree of inhibition provided by the inhibitor.

2.6. Density Functional Theory Calculation

The equilibrium geometry of the complex was studied using DFT calculations at the B3LYP/6-311G+(dp) level of theory, excluding metal ions, performed with the Gaussian 09 program.

2.3. Surface Morphology

The corroded samples' surface topography was analyzed using the SEM and EDX analysis

3. Results and discussion

3.1 Characterization of Al before corrosion

3.1.1 Density measurement

Table 2 displays the relative densities of the consolidated samples. Samples subjected to hot-pressing exhibited the highest densities, while those vacuum-sintered showed the lowest densities [45]. The variation in densities can be attributed to the high-pressure conditions of the hot compaction process during thermo-mechanical consolidation. This process enhances particle interaction, promotes welding between adjacent particles at elevated temperatures, and reduces voids, thereby achieving higher densification [46].

Furthermore, it was observed that increasing the percentage of nickel particles coated with SiC consistently reduced the density. This phenomenon can be attributed to the increased presence of the hard SiC phase during sintering, which limits particle interaction and impedes densification. Favorable densification results across different conditions affirm that the chosen consolidation temperatures were optimal for promoting pressure-induced plastic flow of nickel. Pure Al samples underwent nearly complete densification during sintering, attributed to the small particle size of the powders. Smaller particles have higher surface area and improved diffusion, resulting in densities closer to theoretical values [47].

Composite materials typically undergo different compaction and sintering processes compared to monophasic materials. The possibility of a material decreases when it contains hard, non-deformable particles within a ductile matrix. This effect diminishes as the volume fraction of the reinforcement phase increases [48]. The aluminum matrix surrounding SiC particles experiences more significant deformation, leading to increased porosity (number and size of voids) with higher SiC content. The greater hardness of SiC reduces its compressibility, thereby limiting densification and decreasing the compaction capacity with increasing SiC concentration.

Additionally, it is notable that the density values of mixed SiC with Ni are lower compared to those coated with nickel. This observation can be explained by considering how coating SiC with nano-sized nickel particles enhances their wettability, thereby improving compatibility with the aluminum matrix. Enhanced wettability prevents the formation of gaps between SiC and aluminum in Al-Ni/SiC composites, promoting better interaction among all components and resulting in excellent densification without voids. In contrast, samples reinforced with a mixture of these materials exhibit poor wettability between Al, SiC, and Ni. The heterogeneous distribution of SiC in the Al matrix leads to particle agglomeration and the formation of pores, thereby reducing the density of these samples.

Another notable observation is the gradual decrease in density for both sets of samples with increasing SiC percentages. This phenomenon can be attributed to the increased presence of the hard SiC phase during sintering, which acts as a barrier hindering densification by limiting particle connectivity. Therefore, as the reinforcement component increases, the densification quality of the metal matrix composite decreases due to enhanced SiC particle agglomeration during sintering. Densification is further compromised when the proportion of the disordered phase in the blend is minimized [49]. The

selected consolidation temperature proved optimal for sintering, evident from the generally favorable densification achieved across all compositions. Moreover, composites exhibit reduced densification when the proportion of the deformable phase is reduced. Consolidation at the chosen temperatures facilitated the plastic flow of nickel within the Al matrix under pressure, contributing to successful densification across all compositions. In contrast, pure Al, possessing higher compressibility compared to composites, achieves nearly complete densification in sintered samples.

Moreover, it is noteworthy that samples consolidated by hot compaction exhibit higher density compared to those consolidated by vacuum methods. The limited wettability of SiC and Al composites at temperatures below 1000 °C is well-documented. The presence of residual voids at the interface of the three phases can compromise the characteristics of the samples. In contrast, hot-compacted samples show well-bound three-phase interfaces with minimal visible pores. This can be attributed to the manufacturing technique of hot compaction, where aluminum reaches a semi-liquid state at specific temperatures, facilitating its free flow. Simultaneously, high pressure applied during hot compaction effectively compacts the material. This allows the semi-molten aluminum to easily infiltrate the spaces between SiC particles. Moreover, the process ensures uniform mixing of raw powders, enabling aluminum to achieve a semi-solid and semi-liquid state almost simultaneously, enhancing adhesion to SiC particles. Consequently, hot-compacted samples exhibit a dense microstructure, facilitated by strong interphase bonding [50]. Constraints in the diffusion process contribute to incomplete densification. Reduction in particle size enhances diffusion by increasing surface area, thereby approaching the theoretical density more closely [51].

Table 2. Relative density measurements for Al-(5, 10, and 15%) Ni/SiC for coated and mixed samples.

Samples	Hot compaction mix	Hot compaction coat	Vacuum mix	Vacuum coat
Pure Al	100	100	96.1	98.2
5%	100	99.5	95.6	96.8
10%	98.2	97.5	94.0	95.0
15%	97.0	96.9	91.2	94.2

3.1.2 Hardness Measurements

The impact of plastic deformation on the aluminum composite due to Ni-coated SiC or Ni mixed with SiC was assessed through hardness testing. Table 3 illustrates two phenomena, the first is that adding nickel-coated SiC particles with 5%, 10%, and 15% by weight results in increased hardness. As per the law of mixtures, the composite hardness increased with higher SiC content compared to pure aluminum [52]. Secondly, samples processed by hot pressing exhibit higher hardness values compared to those processed by vacuum sintering. This phenomenon correlates with superior densification as indicated by density data. Thermo-mechanical deformation that occurs during hot compaction induces strain hardening, resulting in dynamically compacted specimens exhibiting higher hardness compared to those produced by traditional or quasi-static compaction methods of the same density. Enhanced work hardening and stronger inter-particle bonding are likely to contribute to this observation. The increased presence of nickel-coated SiC phases, promoting strong adhesion between SiC/Ni and the aluminum phase, likely contributes to the enhanced hardness [53]. The XRD analysis reveals the presence of intermetallic nickel aluminide, further boosting the composite's corrosion resistance and hardness. Additionally, the incorporation of nano-nickel reinforcement increases hardness by 12 HV with the addition of 15% SiC, despite a decrease in density as SiC content rises. This effect is attributed to second-phase hardening [54, 55].

Table 3. Hardness measurements for Al-(5, 10, and 15%) Ni/SiC for coated and mixed samples.

Samples	Hot compaction mix	Hot compaction coat	Vacuum mix	Vacuum Coat
Pure Al	33.1	33.1	25.8	25.7
5%	43.3	35.5	33.7	32.9
10%	43.9	39.9	38.5	41.3
15%	46.0	44.7	41.1	43.0

3.1.3 Phase identification

Figures 2 and 3 display the X-ray diffraction patterns of Al/Ni-SiC composites fabricated through hot pressing and vacuum sintering, respectively. Upon analysis, the composite predominantly comprises aluminum as the primary phase, accompanied by hexagonal SiC and peaks indicating the intermetallic compound Al₃Ni. The presence of nickel and aluminum coating on SiC particles suggests chemical diffusion occurred. During sintering, the phase diagrams of Al and Ni reveal sharp peaks attributable to the Al matrix and Al₃Ni intermetallic, formed between Al and the Ni layer coating SiC particles. Ni effectively encapsulated the SiC particles, as evidenced by the minimal discernibility of SiC peaks. The weak intensity of the SiC peak suggests a substantial incorporation of nickel within the SiC powder. Notably, the consumption of Ni during the synthesis process prevents the observation of Ni peaks.

Figure 2 illustrates peaks corresponding to the primary phase Al and traces of hexagonal SiC detected in the nickel-coated SiC composite samples. Additionally, there are peaks attributable to the Ni₃Al intermetallic, indicating chemical diffusion

between aluminum and nickel ions as per the compound's phase diagram as shown in Fig. 3 [56]. Mixed samples exhibit four phases in their XRD patterns as existed in Fig. 3. Aluminium is the dominant phase, hexagonal SiC with noticeable peaks, significant peaks of Al_3Ni and AlNi_5Si_2 . Coating SiC with nickel explains the subdued peaks due to SiC particles being enveloped in nano-nickel. In contrast, significant peaks are observed in mixed samples where there is no bonding between Al, SiC, and Ni particles. Consequently, intermetallic compounds like Al_3Ni and AlNi_5Si_2 can form through direct reactions involving Al, Ni, and SiC during sintering, corroborated by the phase diagram [56]. It's noteworthy that the AlNi_5Si_2 phase did not form in the hot-pressed samples due to the short processing time, whereas adequate time during vacuum synthesis allowed for its formation.

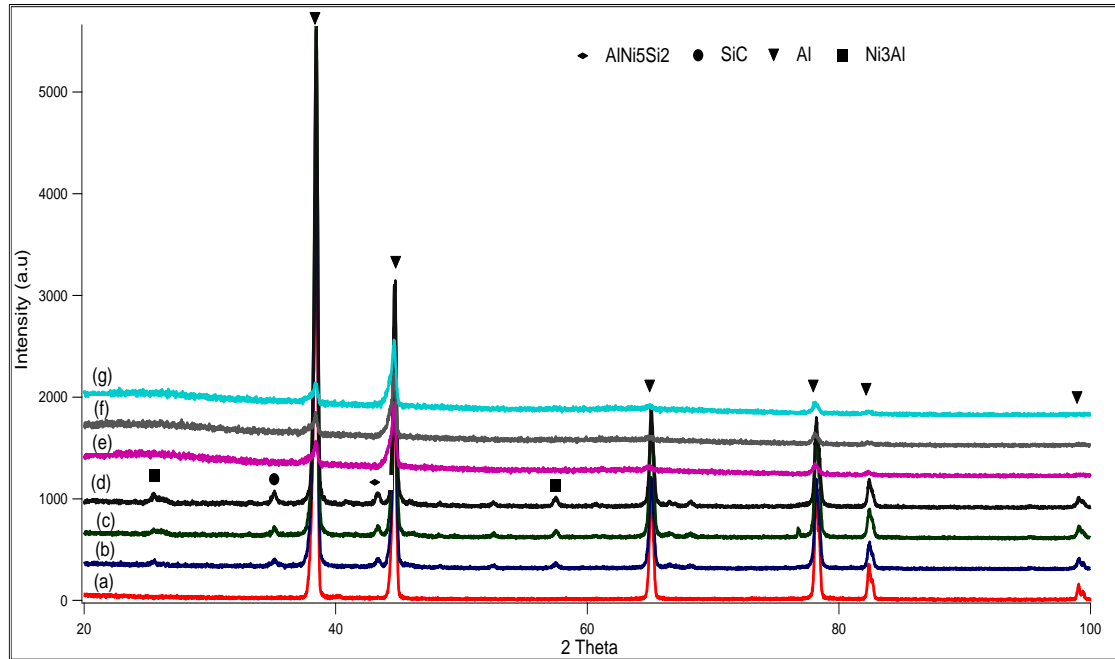


Fig. 2. The XRD analysis for vacuum mixed, (a) pure Al, (b) Al/5%Ni-SiC, (c) Al/10%Ni-SiC, (d) Al/15%Ni-SiC) and vacuum coated Al-Ni/SiC samples, (e) Al/5%Ni-SiC, (f) Al/10%Ni-SiC, (g) Al/15%Ni-SiC) for different conditions.

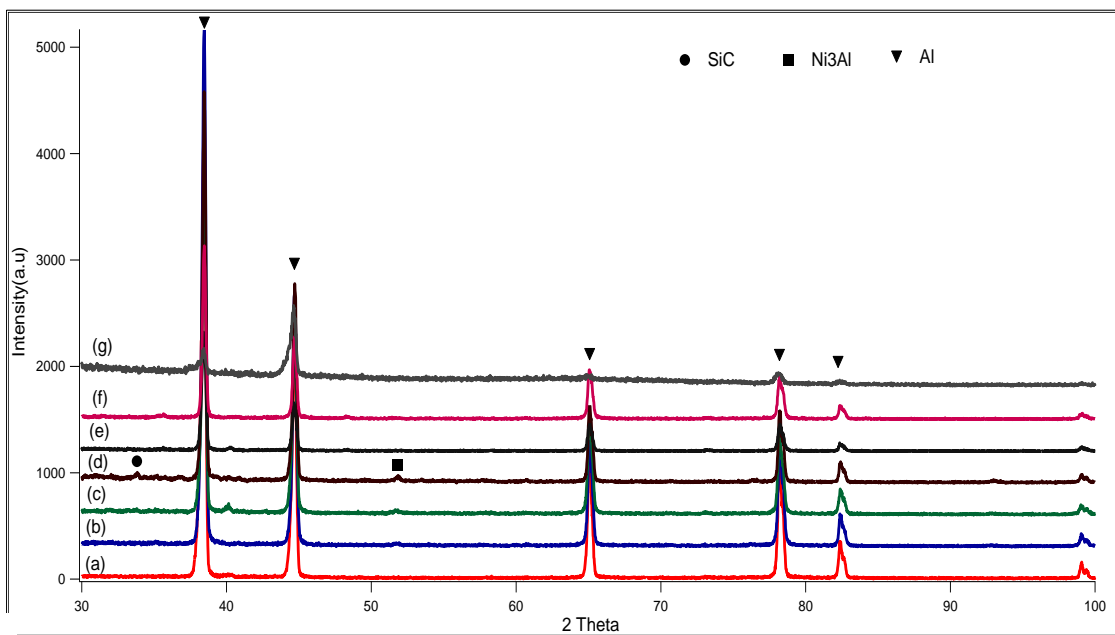


Fig. 3. The XRD analysis for hot compacted mixed (a) pure Al, (b) Al/5%Ni-SiC, (c) Al/10%Ni-SiC, (d) Al/15%Ni-SiC) and hot compacted coated Al-Ni/SiC (e) Al/5%Ni-SiC, (f) Al/10%Ni-SiC, (g) Al/15%Ni-SiC) samples for different conditions.

3.1.4. Microstructure investigation

Figures 4 and 5 display SEM micrographs of hot compacted and vacuum-sintered samples prepared through both mixed and coated samples. The images were captured at high magnification and analyzed using EDX for both the hot-pressed and vacuum-sintered samples. In both techniques, the Ni-coated SiC particles are uniformly distributed throughout the aluminum matrix in the coated samples. This uniform distribution likely results from the process of coating SiC with Ni, which enhances the wettability between SiC and aluminum, facilitating effective coating. The micrographs reveal four distinct phases: the grey Al matrix, white spots representing dispersed Ni phases, dark grey SiC particles, and black spots indicating pores, which increase with higher Ni/SiC fractions. The complete coating of SiC with Ni improves the wettability between Al and SiC, enhancing contact and promoting the complete densification of all samples. Consequently, the presence of pores is minimized.

Furthermore, samples consolidated using different methods display noticeable differences in the microstructure. In vacuum-sintered samples, there is minimal grain development for Ni or SiC particles, and all Ni-coated SiC is uniformly dispersed throughout the Al matrix. Grain boundaries are distinctly visible, likely due to the slow cooling rate during vacuum sintering, facilitating Ni diffusion within the Al matrix and hindering excessive grain growth. Conversely, in hot-pressed samples, grain boundaries are less apparent, and agglomerates of SiC particles are visible. This is attributed to the rapid sintering process and limited control over the heating cycle during hot pressing, which promotes SiC particle clustering rather than uniform dispersion.

The composites coated with Ni display a more even distribution of Ni/SiC particles across the Al matrix, in contrast to the mixed Ni/SiC samples, which exhibit agglomerations and non-uniform distributions. This variation is due to the Ni-coating technique, which encases SiC particles in a nickel film, enhancing their wettability with aluminum. As a result, the Ni-coated SiC particles integrate more closely with the Al matrix compared to the mixed particles. Additionally, including phosphorus (Ni-P) during electroless deposition further improves wettability by reducing the coating thickness. This enhancement leads to variations in particle width and contact area across different composite compositions. The addition of phosphorus to Al matrix composites lowers the contact angle, thereby improving their wetting characteristics [57].

In mixed samples, as the ratio of Ni/SiC particles increased, clustering tendencies among the particles were observed. This clustering led to the formation of voids due to gaps between SiC and Al particles, a characteristic of ceramics like SiC [58]. In contrast, the microstructure of the Al-Ni/SiC composite with Ni-coated SiC particles exhibited better characteristics than that of mixed particles. The Al matrix is represented by the grey phase, scattered Ni particles by the white phase, and SiC particles by the dark grey phase. The presence of dark patches in the mixed samples indicated an increased presence of pores, which became more prevalent with higher Ni/SiC ratios. Overall, the dispersion appears uniform across the entire aluminum matrix [59]. The figures also, illustrate that Ni/SiC particles are uniformly distributed throughout the Al matrix, likely due to the effective mixing of SiC and Ni for an appropriate duration, which improved the wettability between SiC and aluminum.

The pores observed in the distribution of combined Ni/SiC particles throughout the Al matrix can be attributed to their tendency to separate more easily from the matrix. As the proportion of Ni/SiC increased [60], clustering was evident, resulting in voids caused by gaps between SiC and Al particles. Generally, significant variations were found in the microstructure of composites consolidated by two different methods. In hot-pressed samples of Al/Ni-SiC mixes with varying weight percentages, particle sizes remained consistent, which was attributed to optimal conditions for grain growth. Vacuum sintering resulted in well-distributed Ni-SiC in the Al matrix across all samples, with noticeable increases in grain size as the weight percentage increased. It's important to note that reducing the size of SiC particles increased the porosity of the composites. This occurs because during sintering, the diffusion of Al into the matrix and filling of gaps are more challenging with fine SiC particles compared to coarse ones, due to smaller inter-particle gaps. Pores are imperfections that adversely affect mechanical properties, relative density, thermal conductivity, and other composite characteristics. As pore density increases, relative density decreases [61, 62].

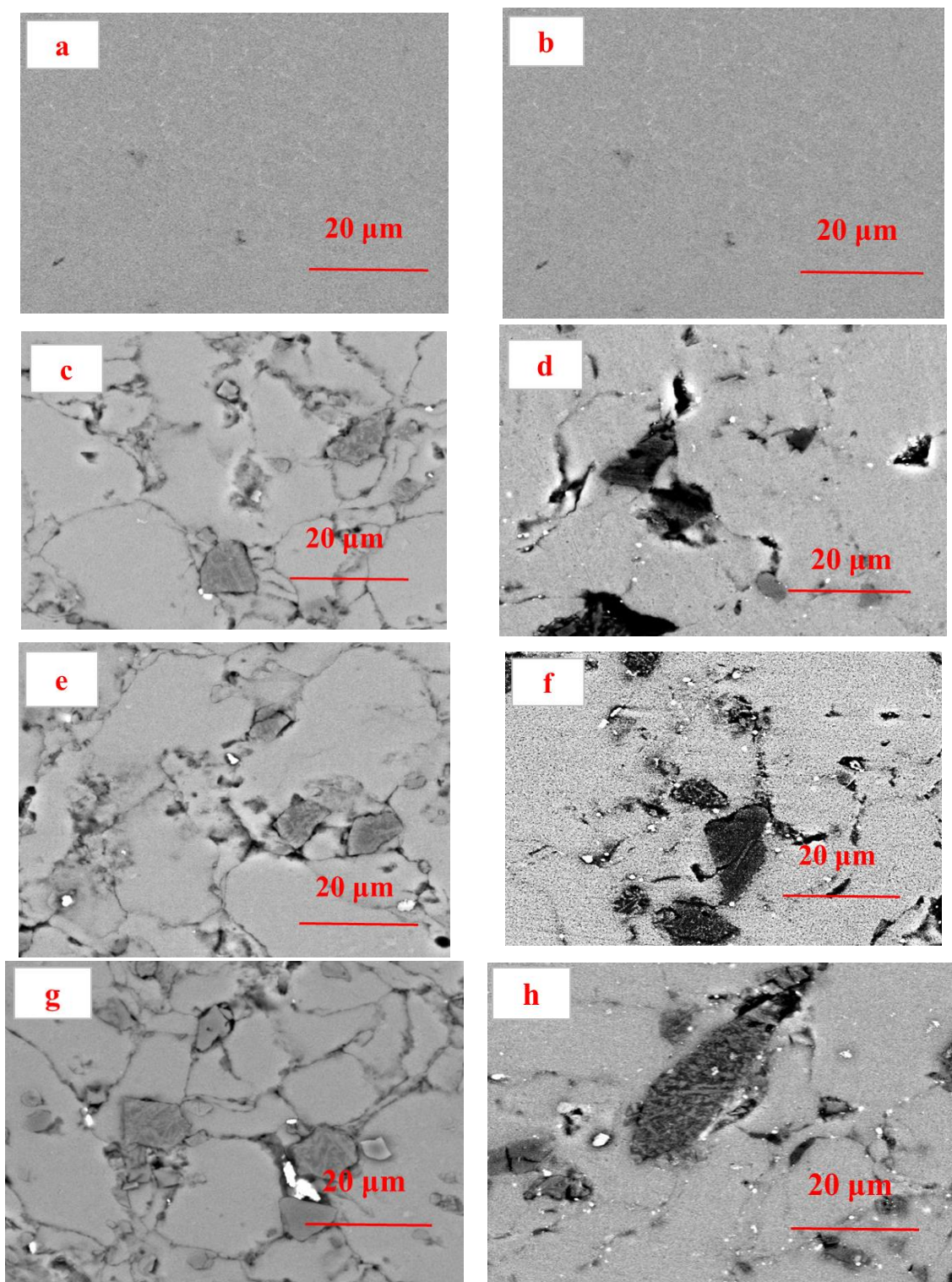


Fig. 4. SEM micrograph for hot compacted samples for mixed samples (a,c, e, g) and coated samples (b, d, f, h).

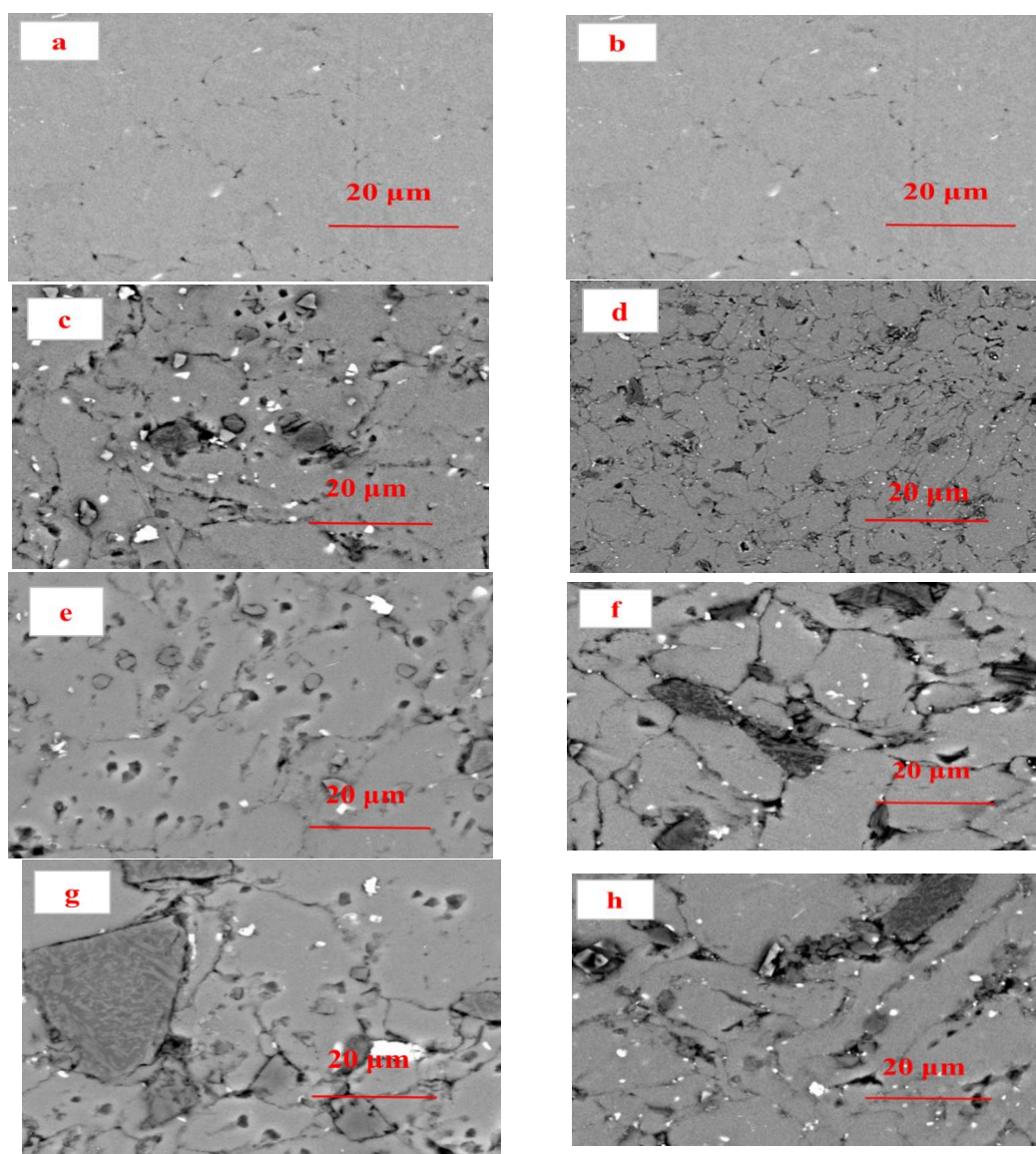


Fig. 5. SEM micrograph for vacuum mixed samples (a, c, e, g) and vacuum coated samples (b, d, f, h).

3.2 Corrosion Behavior

The corrosion resistance of AMMCs presents a significant challenge that limits their widespread adoption. This resistance is heavily influenced by inherent heterogeneities within the composites. Corrosion issues in AMMCs arise from several factors, including galvanic coupling between dissimilar materials, micro-fissures, porosity, voids, and reactive interfacial phases. Despite the potential benefits of AMMCs, research attention on their corrosion behavior has been relatively limited compared to other aspects of composite materials. To investigate the corrosion behavior of AMMCs, researchers employ various testing methods such as PDP experiments and immersion studies. However, to advance their practical applications, further research into the underlying mechanisms of AMMC corrosion is essential.

3.2.1. Weight loss (WL) measurements

3.2.1.2 Effect of Treatment Time

In Fig. 6, the corrosion behavior of Al/Ni-SiC composites under various sintering conditions in 1M HCl is illustrated. With increasing immersion time, more corrosion products accumulated on the composites, yet fewer detached corrosion products indicated a slowed CR. The combination of sealing with anodic oxidation notably enhanced surface resistance, evidenced by the lowest loss observed. The CR values, measured by WL after 120 h of immersion, are summarized in Table 4. The CR decreased with increasing concentrations (5%, 10%, and 15%) of nickel-coated SiC particles by weight. The CR values of 15% nickel-coated SiC particles were 1.17 mm/y for hot compaction and 0.39 mm/y for vacuum mixing in 1M HCl.

Another study investigated the corrosion behavior of Al2024-TiC-MMC in a 3.5% NaCl solution, revealing that higher anodic current densities reduced the size and number of pits due to increased hydrogen diffusion rates. Stress corrosion

cracking (SCC) characteristics were assessed using a double cantilever specimen immersed in artificial seawater, where higher annealing temperatures led to lower dislocation density and stable propagation rates, alongside an increased threshold stress intensity factor influencing SCC propagation rates significantly. Additionally, the PDP method was employed at 25°C in a de-aerated neutral 3.5% NaCl solution to investigate the corrosion behavior of Al 2009/SiCp composites [63]. Another extensive study focused on a powder-processed Al-Si-Mg-SiCp composite with low scandium content, highlighting increased pitting behavior in the presence of a 3% NaCl solution compared to a 0.1% NaCl solution [64]. Corrosive attack in Al/SiCp composite materials is typically initiated at the interfacial layers of matrix/SiCp and matrix/intermetallic phases, as observed in studies examining the pitting phenomenon in AMMCs [65].

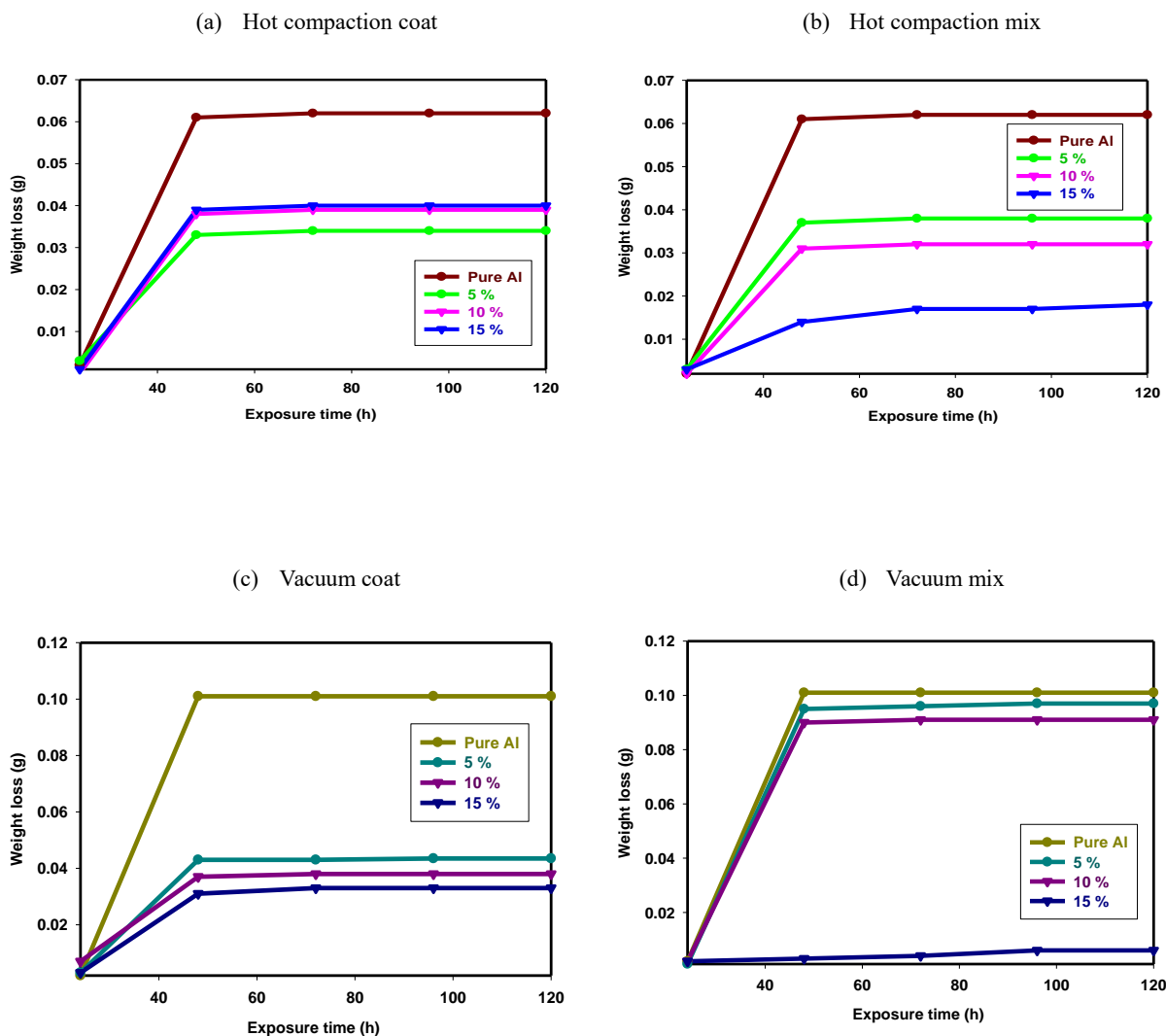


Fig. 6. The WL-time curves for Al/Ni-SiC composites in 1M HCl at a temperature of 25 °C.

Table 4. The WL and CR values of Al/Ni-SiC composites in 1M HCl for 120 h at a temperature of 25 °C by the WL method.

Samples	Hot compaction coat		Hot compaction mix		Vacuum coat		Vacuum mix	
	WL g	CR mm/y	WL g	CR mm/y	WL g	CR mm/y	WL g	CR mm/y
Pure Al	0.062	4.04	0.062	4.04	0.101	6.58	0.101	6.58
5 %	0.034	2.22	0.038	2.48	0.044	2.83	0.097	6.32
10 %	0.039	2.54	0.032	2.08	0.038	2.48	0.091	5.93
15 %	0.040	2.61	0.018	1.17	0.033	2.15	0.006	0.39

3.2.2. PDP measurements

3.2.2.1. Effect of corrosive media on Al/Ni-SiC composite

In Fig. 7, the PDP curves of the Al/Ni-SiC composite in 1M HCl are depicted. Tables 5, 6, 7, and 8 summarize corrosion metrics including E_{corr} , β_a , β_c , I_{corr} , and CR. The vacuum-mixed composite shows a CR of 0.77 mm/y, while the hot-compact composite with a 15% Al/Ni-SiC coating exhibits a rate of 2.76 mm/y. Corrosion in aluminum-based composites primarily involves pitting that initiates at the interface of the MMC. Samples coated with 5%, 10%, or 15% Al/Ni-SiC and consolidated by hot compaction or vacuum sintering displayed higher potential values compared to the base alloy. The matrix structure of Al2024-SiC composites or the base alloy, however, remained unaffected [66]. Comparisons between Al6061-SiC composites and SiC-reinforced Al6061-T6 indicate better corrosion resistance in the latter [67]. Pitting initiation was also observed to be higher in Al6061 MMCs reinforced with SiC whiskers compared to the base alloy, with increased cathodic currents attributed to the interfacial layer [68].

Another study investigating the polarization behavior of Al1050 reinforced with SiCp particles of 3 μ m and 30 μ m found that the composites were more susceptible to pitting attacks than the base alloys due to gaps at the reinforcement-matrix interface. However, the polarization behavior was unaffected by residual stresses between reinforcements and the matrix. Localized corrosion was more prevalent in SiCp with a size of 20 μ m compared to those with 60 μ m, as noted in previous studies [69, 70].

In a study examining localized corrosion effects, researchers found that Al2024-SiCp MMCs with SiCp particles sized at 14 μ m and varying volume fractions exhibited inferior corrosion resistance compared to the unreinforced base alloy. The study noted an increase in active sites on the composite surface and a decrease in pitting potential as the volume fraction of SiCp in the MMC increased [71]. Additionally, the research indicated that the inclusion of SiCp accelerated the CR of the composites [72, 73].

Table 5. Corrosion parameters of Al/Ni-SiC hot compaction coat in 1M HCl at a temperature of 25 °C.

Hot compaction coat	E_{corr} mV	I_{corr} mA/cm ²	β_a mV/dec	β_c mV/dec	CR mm/y
Pure Al	-710.8	0.4380	101.5	-303.5	5.12
5 %	-661.6	0.1606	116.0	-301.2	1.88
10 %	-662.2	0.3408	147.5	-307.5	3.99
15 %	-694.9	0.3863	141.3	-273.9	4.52

Table 6. Corrosion parameters of Al/Ni-SiC hot compaction mix in 1M HCl at a temperature of 25 °C.

Hot compaction mix	E_{corr} mV	I_{corr} mA/cm ²	β_a mV/dec	β_c mV/dec	CR mm/y
Pure Al	-710.8	0.4380	101.5	-303.5	5.12
5 %	-688.6	0.3322	132.3	-265.5	3.89
10 %	-668.0	0.2447	142.5	-262.6	2.86
15 %	-639.8	0.2360	142.5	-262.2	2.76

Table 7. Corrosion parameters of Al/Ni-SiC vacuum coat in 1M HCl at a temperature of 25 °C.

Vacuum coat	E_{corr} mV	I_{corr} mA/cm ²	β_a mV/dec	β_c mV/dec	CR mm/y
Pure Al	-719.4	0.43760	82.7	-312.0	5.12
5 %	-646.9	0.18208	130.7	-164.9	2.13
10 %	-622.1	0.12828	108.9	-256.0	1.50
15 %	-558.1	0.11654	184.3	-304.7	0.94

Table 8. Corrosion parameters of Al/Ni-SiC vacuum mix in 1M HCl at a temperature of 25 °C.

Vacuum mix	E_{corr} mV	I_{corr} mA/cm ²	β_a mV/dec	β_c mV/dec	CR mm/y
Pure Al	-719.4	0.43760	82.7	-312.0	5.12
5 %	-651.0	0.23360	142.4	-283.6	2.73
10 %	-634.9	0.20392	160.5	-213.2	2.39
15 %	-630.8	0.15110	162.1	-175.7	0.77

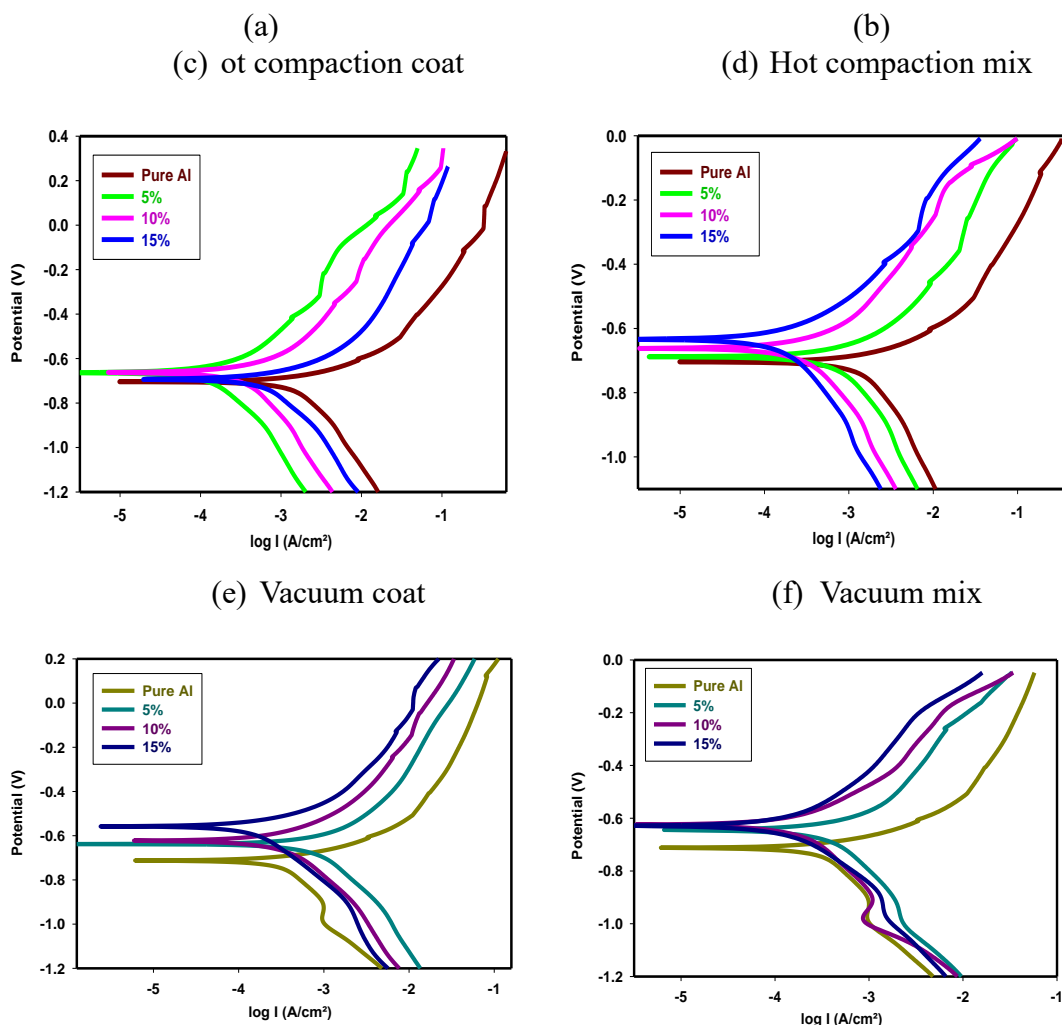


Fig.7. The PDP curves of Al/Ni-SiC composites in 1M HCl at a temperature of 25 °C

3.3. Corrosion Inhibitors

Extending the longevity of Al/Ni-SiC composites hinges significantly on thwarting corrosion. Researchers have investigated diverse strategies such as anodizing and applying different coatings to bolster these composites' resistance to corrosion. To mitigate pitting corrosion, studies have also examined the efficacy of corrosion inhibitors in Al/Ni-SiC composites. Implementing corrosion inhibitors can effectively enhance the composite's durability by fortifying its resistance against corrosive threats [74].

3.3.1 Effect of Treatment Time on Inhibition of Al/Ni-SiC

The corrosion performance of Al/Ni-SiC composites subjected to various sintering processes in 1M HCl containing 100 ppm CuL₂ nanocomplex at 25°C was examined concerning immersion time as represented in Fig. 8 and Table 9. At 72 hours, there was a slight improvement in the protection efficiency when the immersion period was increased. As a protective film gradually forms on the surface of the Al/Ni-SiC composite electrodes, the protection efficiency values start to rise. A more efficient and long-lasting protective layer is formed as the immersion period increases through the interaction of the corrosion inhibitor (CuL₂ nanocomplex) with the composite material. The composite's corrosion resistance is improved over time by this protective film's barrier effect, which hinders the corrosive attack. The nickel-coated SiC particles' CR values in the hot compaction mix fell from 1.17 mm/y to 1.11 mm/y and in the vacuum mix at 15% in 1M HCl from 0.39 mm/y to 0.33 mm/y, respectively, when the CuL₂ nanocomplex was not present.

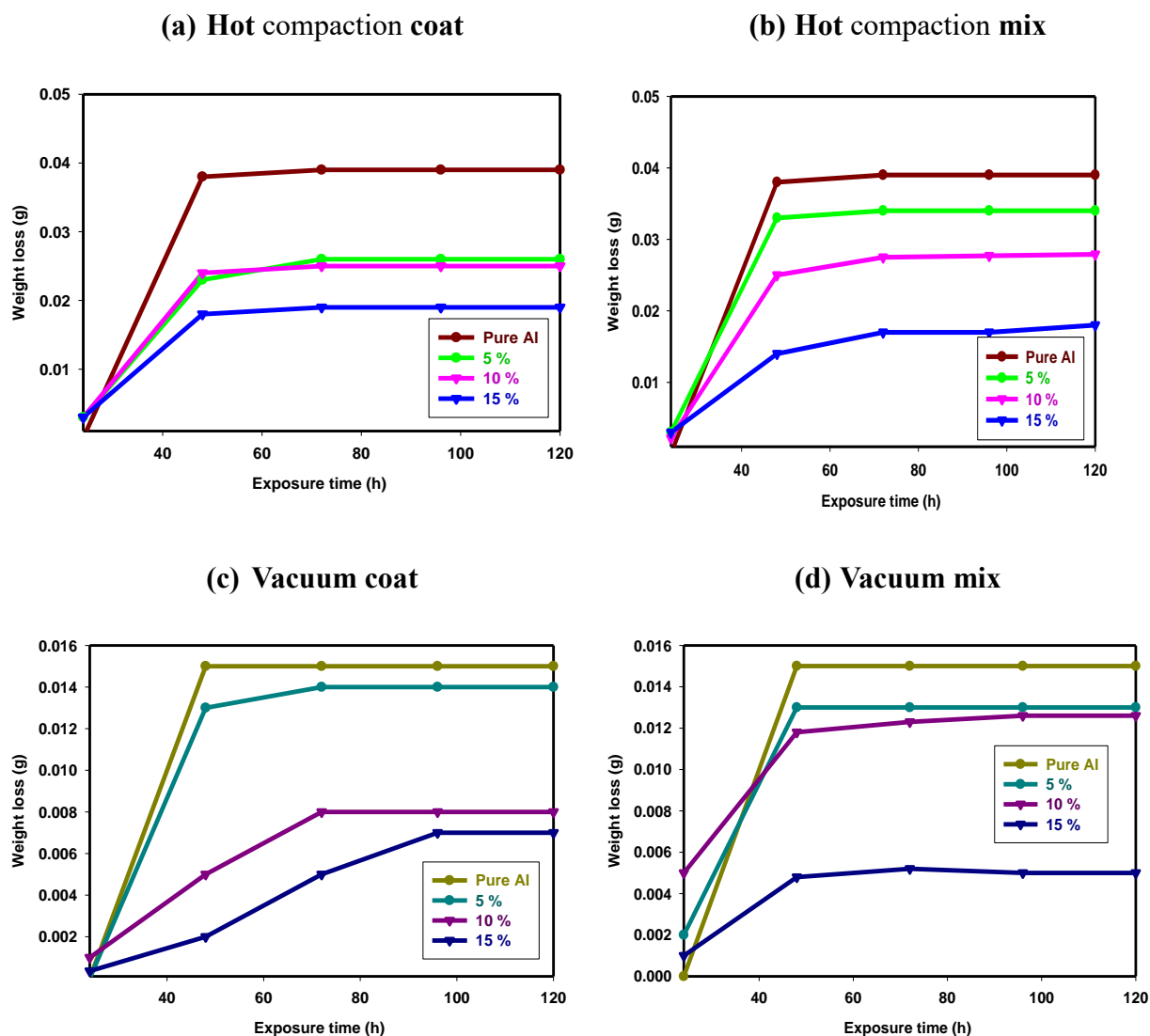


Fig. 8. The WL-time curves for Al/Ni-SiC composites in 1M HCl in the absence and presence of CuL₂ nanocomplex at a temperature of 25°C.

Table 9. The CR values and inhibition efficiency for Al/Ni-SiC composite in 1M HCl with 100 ppm CuL₂ nanocomplex for 120 h at a temperature of 25 °C by WL method.

Samples	Hot compaction coat		Hot compaction mix		Vacuum coat		Vacuum mix	
	WL g	CR mm/y	WL g	CR mm/y	WL g	CR mm/y	WL g	CR mm/y
Pure Al	0.039	2.54	0.039	2.54	0.015	0.98	0.015	0.98
5 %	0.026	1.69	0.034	2.22	0.014	0.91	0.013	0.85
10 %	0.025	1.63	0.028	1.82	0.008	0.52	0.013	0.82
15 %	0.019	1.24	0.017	1.11	0.007	0.46	0.005	0.33

3.3.2. Effect of Inhibitor Concentration on Al/Ni-SiC Composite

The weight reduction procedure results for different concentrations of CuL₂ nanocomplex are summarized in Table 10 and Fig. 9, detailing CR and percentage inhibition efficiency (IE%) at 25°C. Notably, the highest corrosion protection efficacy for Al/Ni-SiC was observed at a concentration of 600 ppm CuL₂ nanocomplex. This effect is attributed to the formation of a protective film on the electrode surface facilitated by the presence of CuL₂ nanocomplex. This protective film acts as a barrier

at the interface between the composite material and the corrosive environment, effectively reducing the rate of electron transfer and thereby enhancing protection efficiency against corrosion, leading to a significant decrease in CR.

The study demonstrates effective inhibition of Al/Ni-SiC corrosion in 1M HCl across CuL₂ nanocomplex concentrations ranging from 100 to 600 ppm. As depicted in Fig. 9, the CR (mm/y) steadily declines with increasing inhibitor concentration. Passivation is achieved after 72 h, where the WL of Al/Ni-SiC reaches its minimum due to the acidic solution initially dissolving the material and subsequently forming a protective oxide layer on its surface. The CuL₂ nanocomplex further enhances passivation, maintaining the protective oxide layer for an extended period, effectively shielding Al/Ni-SiC from further corrosion. These findings underscore the potential of CuL₂ nanocomplex as a robust inhibitor against acidic corrosion in Al/Ni-SiC composites.

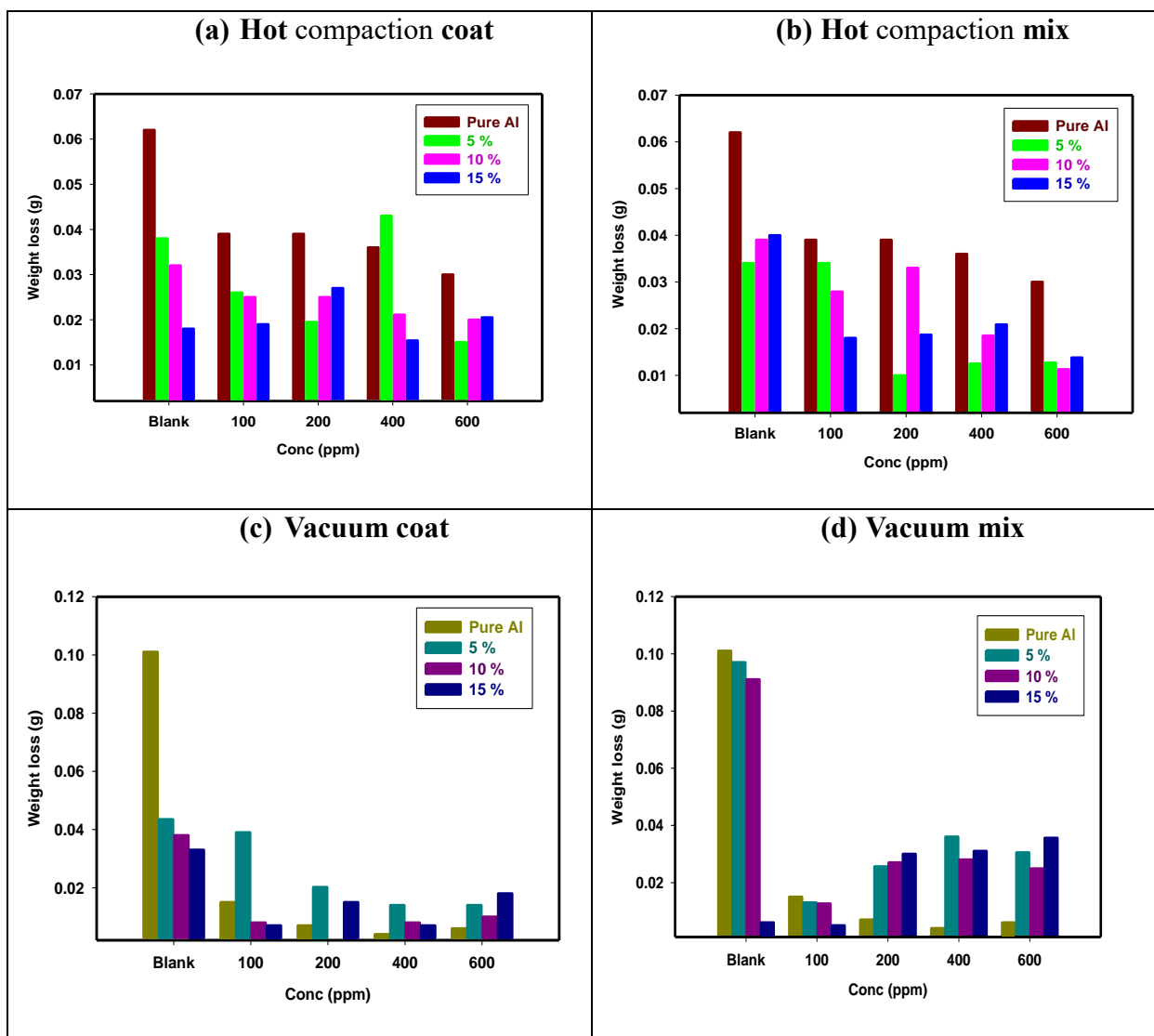


Fig. 9. The WL curves via different concentrations of Al/Ni-SiC composite in 1M HCl with CuL₂ nanocomplex at a temperature of 25 °C.

3.3.3. PDP of CuL₂ nanocomplex on Al/Ni-SiC Composite

Figure 10 depicts the PDP curves of the Al/Ni-SiC composite in 1M HCl, comparing conditions with and without CuL₂ nanocomplex. Tables 10, 11, 12, and 13 provide detailed corrosion characteristics such as E_{corr} , β_a , β_c , I_{corr} , and CR values. Research investigating synergistic inhibitors on Al/Ni-SiC composites in 1M HCl solutions demonstrates that CuL₂ nanocomplex-coated Al/Ni-SiC composites exhibit enhanced corrosion protection compared to their uncoated counterparts. This enhanced protection is attributed to the presence of SiC particles within the Al/Ni-SiC composite [74]. Similarly, studies exploring various coatings—K₂Cr₂O₇, Sodium molybdate, and Cerium chloride—on Al6013/SiCp composites in 3.5% NaCl solutions found that cerium chloride treatment provides the highest corrosion resistance among the coatings examined. Additionally, micro-arc oxidation (MAO)-produced anti-corrosion layers on Al2024/SiCp composites demonstrated effective suppression of corrosion in 3.5% NaCl solutions [75].

The data also indicate that the incorporation of 5%, 10%, and 15% CuL₂ nanocomplex -coated Al/Ni-SiC samples results in decreased I_{corr} values, which further decrease with the addition of CuL₂ nanocomplex. This reduction in I_{corr} is attributed to the adsorption of inhibitor molecules onto the Al/Ni-SiC composite, which blocks active sites on the surface and hinders both anodic and cathodic processes. The shift in E_{corr} towards more positive values, though less than 85 mV, suggests that the effects of Al/Ni-SiC coating and CuL₂ nanocomplex are of a mixed nature. Moreover, the CR values of nickel-coated SiC particles in hot compaction and vacuum mixes at 15% in 1M HCl decreased from 2.76 mm/y to 2.26 mm/y and from 0.77 mm/y to 0.26 mm/y, respectively, in the presence versus absence of CuL₂ nanocomplex.

Table 10. Corrosion parameters of Al/Ni-SiC in 1M HCl in the presence of CuL₂ nanocomplex manufactured by hot compaction coat at a temperature of 25 °C.

Hot compaction coat inh	E_{corr} mV	I_{corr} mA/cm ²	β_a mV/dec	β_c mV/dec	CR mm/y	θ
Pure Al	-768.6	0.18307	186.5	-187.0	2.14	58.2
5 %	-635.6	0.27950	129.9	-183.9	3.27	15.9
10 %	-628.4	0.18707	134.5	-188.8	2.19	23.5
15 %	-605.3	0.19288	154.9	-230.5	2.26	18.3

Table 11. Corrosion parameters of Al/Ni-SiC in 1M HCl in the presence of CuL₂ nanocomplex manufactured by hot compaction mix at a temperature of 25 °C.

Hot compaction mix inh	E_{corr} mV	I_{corr} mA/cm ²	β_a mV/dec	β_c mV/dec	CR mm/y	Θ
Pure Al	-768.6	0.18307	186.5	-187.0	2.14	58.2
5 %	-607.5	0.08830	115.5	-216.5	1.03	45.0
10 %	-668.5	0.12028	154.7	-150.7	1.41	64.7
15 %	-571.4	0.11071	125.5	-201.3	1.39	69.2

Table 12. Corrosion parameters of Al/Ni-SiC in 1M HCl in the presence of CuL₂ nanocomplex manufactured by vacuum coat at a temperature of 25 °C.

Vacuum coat inh	E_{corr} mV	I_{corr} mA/cm ²	β_a mV/dec	β_c mV/dec	CR mm/y	Θ
Pure Al	-714.2	0.27870	106.3	-299.0	3.26	36.3
5 %	-609.4	0.09063	124.9	-209.6	1.06	50.2
10 %	-627.0	0.09716	116.0	-120.2	1.14	24.3
15 %	-655.1	0.06695	157.7	-195.4	0.78	16.3

Table 13. Corrosion parameters of Al/Ni-SiC in 1M HCl in the presence of CuL₂ nanocomplex manufactured by vacuum mix at a temperature of 25 °C.

Vacuum mix inh	E_{corr} mV	I_{corr} mA/cm ²	β_a mV/dec	β_c mV/dec	CR mm/y	θ
Pure Al	-714.2	0.2787	106.3	-299.0	3.26	36.3
5 %	-638.3	0.2248	143.7	-188.5	2.63	3.8
10 %	-616.9	0.1299	157.8	-166.1	1.52	36.3
15 %	-642.1	0.0220	109.6	-180.2	0.26	66.4

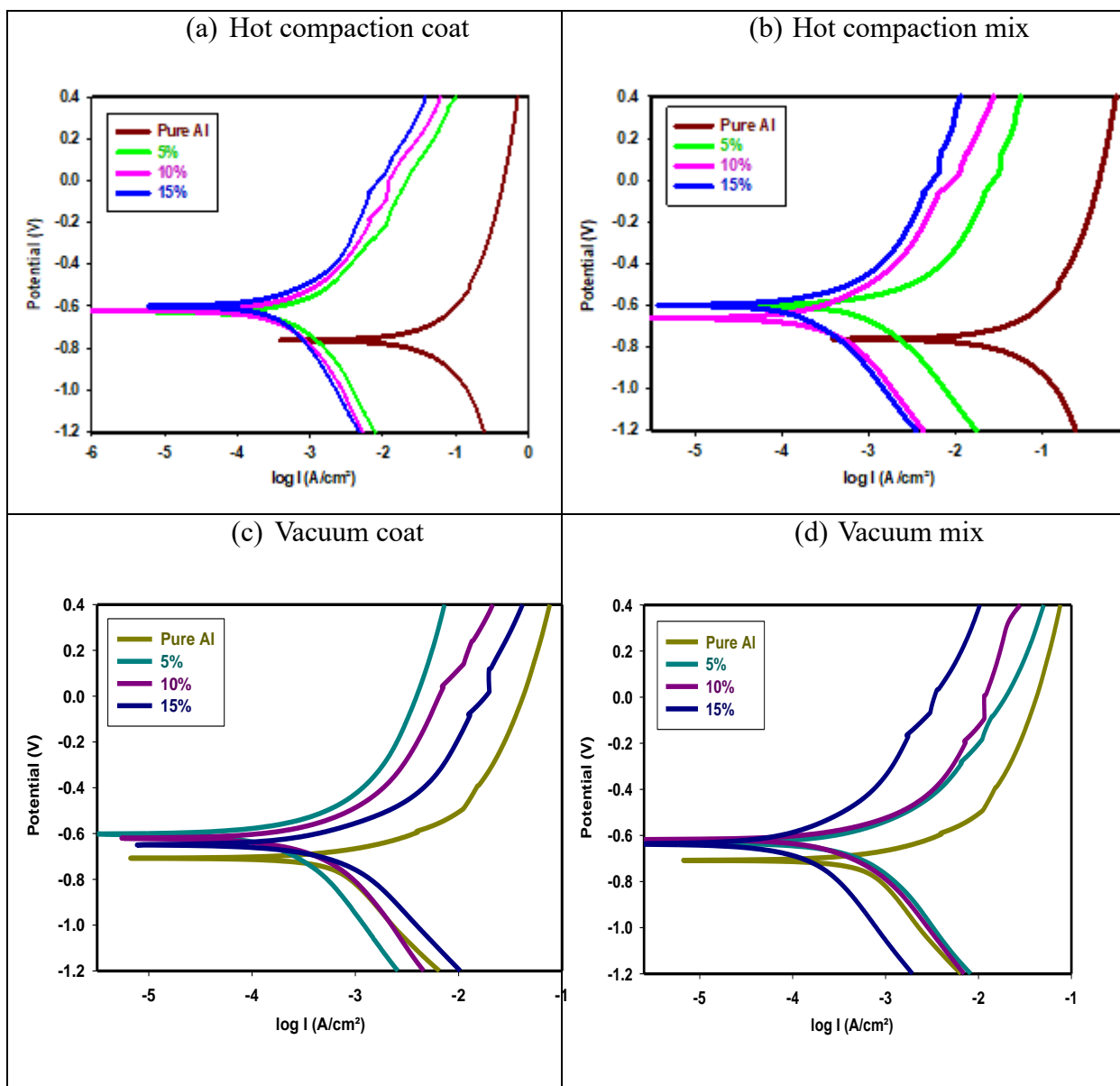


Fig. 10. The PDP curves of Al/Ni-SiC in 1M HCl in the absence and presence of CuL_2 nanocomplex at a temperature of 25 °C.

The CR values for the coated samples prepared by hot compaction and vacuum sintered samples are lower than those for the mixed samples prepared by the same techniques, respectively. This may be due to the high appearance of ceramic SiC particles in the mixed samples compared to the coated ones, which have high corrosion resistance compared to Al and Ni metals. The complete capsulation for SiC with Al and Ni elements is subjected to the corrosive medium, in contrast to the mixed sample, where SiC is subjected also to the same condition. Additionally, both the vacuum coat and vacuum mix exhibit lower CR values compared to the hot compaction coat and hot compaction mix, despite having lower density. This can be explained by the vacuum technique producing a new phase, AlNi_5Si_2 , which may be causing the decrease in CR.

3.3 Surface Morphology

Figures 11 and 12 display SEM images and EDX results of the corroded samples without inhibitors. Figures 13 and 14 present SEM images and EDX analyses of the samples treated with inhibitors. Specifically, Figures 11(a) and (b) show the protective layers of the hot compaction and vacuum mixed samples, respectively, while Figures 11(c) and (d) provide detailed views of these protective layers. The CR values reported in Tables 5-8 align with these observations. Comparatively, Figures 12(a) and (b) indicate higher oxygen percentages than Figures 12(c) and (d), these are related to hot compaction-coated samples and vacuum coated without inhibitor additions, respectively.

Figures 13 and 14 demonstrate that the addition of the inhibitor exhibits a similar trend to the conditions without it. However, the values are generally lower with the inhibitor, which correlates with the CR values reported in Tables 10-14.

SEM images in Figures 13(a), (b), and (d) reveal some cracks, which correspond to the increased oxygen percentages observed in Figures 14(a), (b), and (d), these are related to hot compaction coat, vacuum coat, vacuum mix with inhibitor additions. This could indicate the initial formation of new protective layers.

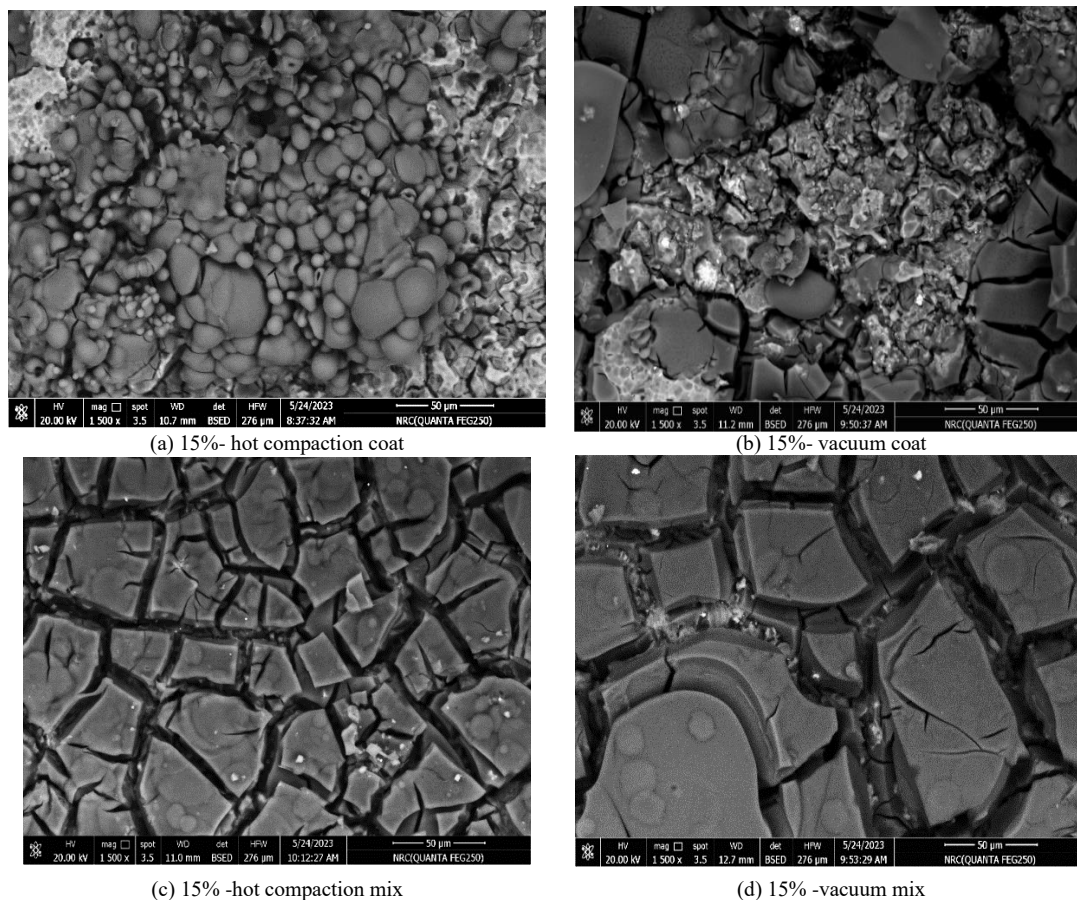


Fig. 11. The SEM images of corroded samples without inhibitor.

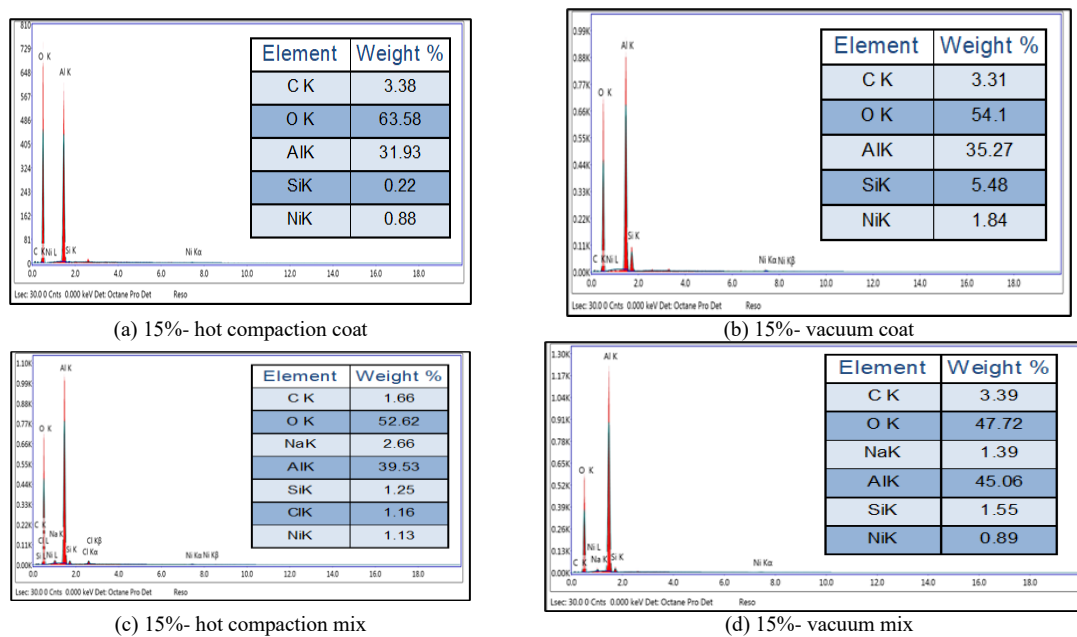


Fig. 12. The EDX patterns of corroded samples without inhibitor.

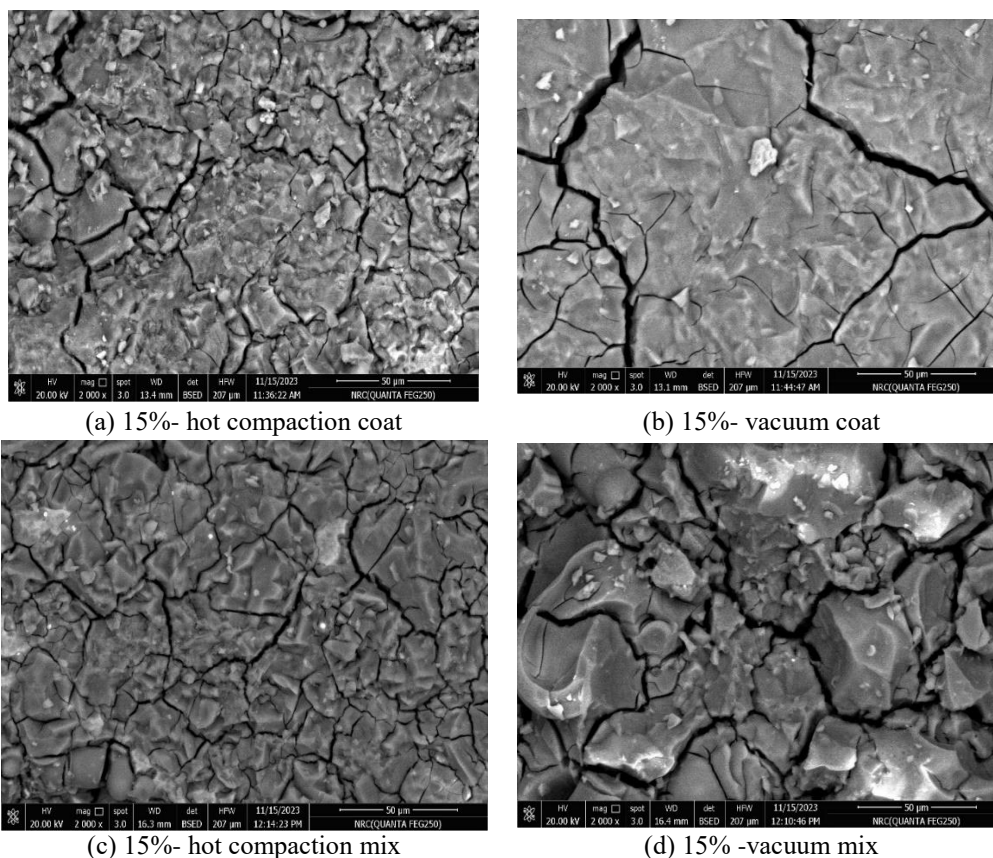


Fig. 13. The SEM images of corroded samples with inhibitor.

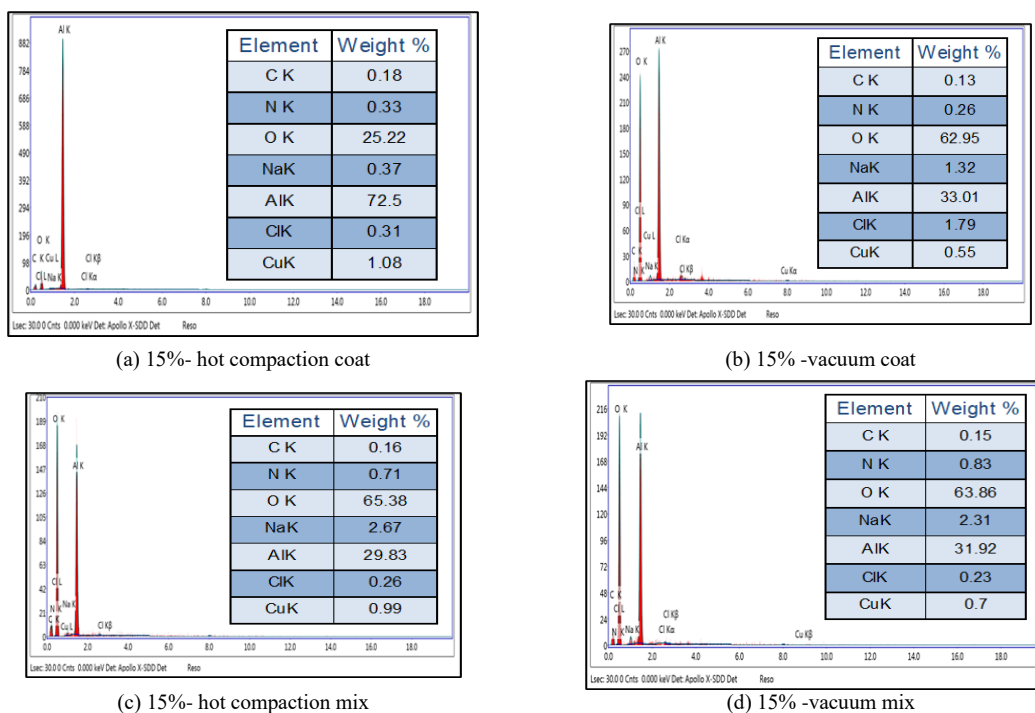


Fig. 14. The EDX patterns of corroded samples with inhibitor.

3.4. DFT parameters and inhibitor efficiency relationship

Theoretical analysis, often through DFT, is a common method for inferring corrosion mitigation mechanisms. Figure 15 presents the result of a theoretical investigation using DFT to assess the efficacy of a synthesized CuL_2 nanocomplex as a green inhibitor. The molecular structure of an inhibitor plays a crucial role in its effectiveness. The frontier orbital model is

employed to predict where additive compounds attract to adsorption centers. Effective inhibitors are those capable of both donating electrons to and accepting electrons from Al/Ni-SiC composites [77, 78]. The mitigation mechanism is inferred by analyzing the HOMO (highest occupied molecular orbital) and LUMO (lowest unoccupied molecular orbital) of the synthesized nano complex. Compounds with a high HOMO energy level can donate electrons to empty acceptor orbitals, while E_{LUMO} represents the ability to accept electrons [79]. Figure 16 and Table 14 depict geometric structures and the locations of LUMO and HOMO. Two mechanisms are involved in the adsorption of inhibitor molecules onto the Al/Ni-SiC composite interface: coordinate bonding, where the inhibitor's electrons fill empty d-orbitals of the metal surfaces; and back-bonding, where the inhibitor accepts electrons from atoms on the surface.

Previous studies have shown that inhibitors with lower energy gaps (ΔE) between E_{HOMO} and E_{LUMO} tend to exhibit higher protection efficiencies due to easier electron transfer. Based on E_{HOMO} , E_{LUMO} , and ΔE findings, the CuL₂ nanocomplex demonstrates moderate corrosion inhibition effectiveness [78]. Table 15 further explores the interaction between inhibitor molecules and metal surfaces, discussing parameters such as global hardness (η), global softness (σ), electronegativity (X), chemical potential (μ), global electrophilicity (ω), and energy of back-donation (E_{b-d}). The methodologies employed in these calculations are detailed in previously published works [39, 80], where the relationships utilized are also described [40, 81].

An inhibitor is deemed highly effective and chemically reactive if it exhibits a high softness value and low global hardness [81]. Furthermore, the stability of nanocomplexes is indicated by their negative chemical potential values, as shown in Table 1. With a higher softness (s) value and lower global hardness (η), the CuL₂ nanocomplex is more likely to adsorb onto metal substrates. The negative value of E_{b-d} suggests that the inhibitor benefits energetically from back-donation by the metal. Both back donation and acceptance mechanisms enhance the adsorption of inhibitors onto metal surfaces, contributing to their effectiveness in laboratory settings. Fig. 17 illustrates how the distribution of charges and the reactivity of inhibitor compounds can be predicted using the molecules' electrostatic potential [82]. In this representation, the blue regions of the CuL₂ nanocomplex indicate areas where electrons are likely to be found, while the red regions signify sites prone to nucleophilic attack.

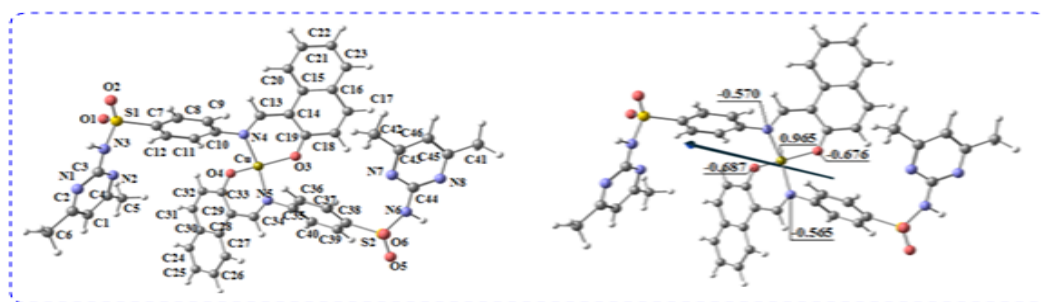


Fig. 15. The inhibitor's optimized structure, dipole moment vector, and natural charges on CuL₂ nanocomplex active centers [41].

Table 14. Inhibitor of CuL₂ nanocomplex derived from quantum chemical calculations.

Parameters	CuL ₂ nanocomplex
Total energy, (Hartree)	- 3657.610
Dipole moment, (Debye)	4.8415
Chemical potential μ , (eV)	- 4.6881
electronegativity X , (eV)	4.6881
E_{HOMO} , (eV)	- 5.6720
E_{LUMO} , (eV)	- 3.7041
ΔE , (eV)	1.9679
η , (eV)	0.9840
σ , (eV ⁻¹)	1.016
Ω	11.168
E_{b-d} (eV)	-0.246

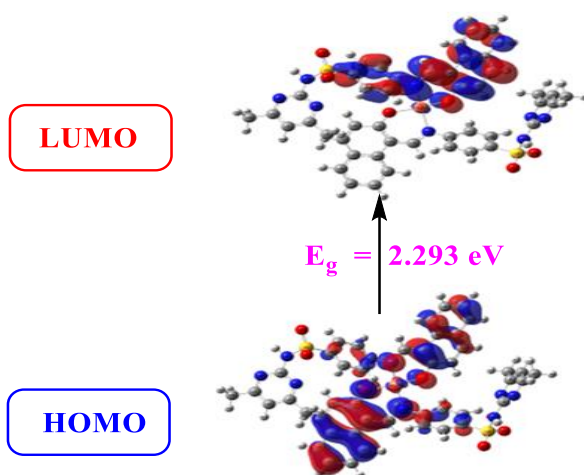


Fig. 16. Exploring the MO and their energies as inhibitors of CuL_2 nanocomplex.

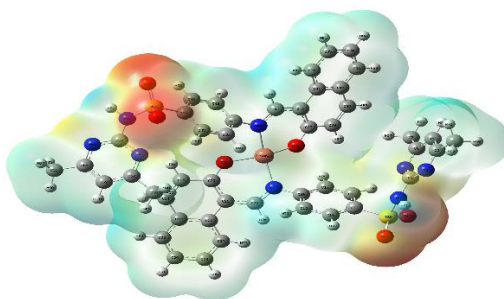


Fig. 17. Copper nanocomplex inhibitor molecular electrostatic potential (MEP) surface.

4. Conclusions

The corrosion performance of Al/Ni-SiC composites prepared by powder metallurgy techniques is discussed, emphasizing the significance of their electrochemical and chemical properties. It was concluded the following:

1. Electrochemical studies, including potentiodynamic polarization curves, revealed that the addition of CuL_2 nanocomplex as an inhibitor led to a reduction in the CR and an increase in the corrosion resistance of the composites.
2. The presence of CuL_2 nanocomplex resulted in the formation of a protective film on the surface of the Al/Ni-SiC composites, which inhibited the electrochemical reactions responsible for corrosion.
3. The corrosion rate decreased with increasing concentrations (5%, 10%, and 15%) of nickel-coated SiC particles by weight. The nickel-coated SiC particles in the hot compaction mix and vacuum mix at 15% in 1M HCl exhibited CR values of 1.17 mm/y and 0.39 mm/y, respectively.
4. Chemical analyses, such as SEM and EDX, provided insights into the morphology and elemental composition of the corroded samples. Comparisons between samples with and without inhibitors highlighted the effectiveness of CuL_2 nanocomplex in mitigating corrosion.

Overall, the combination of electrochemical and chemical analyses elucidated the corrosion behavior of Al/Ni-SiC composites and demonstrated the potential of CuL_2 nanocomplex as a corrosion inhibitor for these materials.

Declaration of Competing Interest

There are no conflicts to declare.

References

- [1]. M.K. Surappa, Aluminium Matrix Composites: Challenges and Opportunities Sadhana. Department of Metallurgy, Indian Institute of Science, Bangalore 560 012, India 28 (2003) 319–334
- [2]. R.A. Kumar, S.J. Akash, S. Arunkumar, V. Balaji, M. Balamurugan, A.J. Kumar, Fabrication and Corrosion Behaviour of Aluminium Metal Matrix Composites – A Review, IOP Conf. Series: Materials Science and Engineering 923 (2020) 012056.
- [3]. R.A. Kumar, A. Devaraju, S. Arunkumar, Experimental Investigation on Mechanical Behaviour and Wear Parameters of TiC and Graphite Reinforced Aluminium Hybrid Composites 5 (2018).

- [4]. S.S. Ganesh, A. Jegan, Response surface methodology optimization of pulse electrodeposited Ni- nano SiC coatings on Al 7075 substrate, *Journal of Ceramic Processing Research*. Vol. 24, No. 3, pp. 486–494 (2023).
- [5]. T. Dursun, C. Soutis, Recent developments in advanced aircraft aluminium alloys, *Mater. Des.* 56 (2014) 862–871.
- [6]. G.A. Gaber, W. A. Hussein, and W. A. Ghanem, “Nanoparticles deposition effects on 1050A aluminum alloy anodic layers,” *Mater. Res. Express*, 7(1) (2020) 16567.
- [7]. G. A. Gaber, L.Z. Mohamed, W. Abd-Elaziem, Influence of Different Processes on Corrosion Performance of Al 1070 Alloy in Chloride Media, *Egypt. J. Chem*, 67(9) (2024) 589–600.
- [8]. B. Kaveendran, G.S. Wang, L.J. Huang, L. Geng, H.X. Peng, In situ (Al₃Zr + Al₂O₃np)/2024Al metal matrix composite with novel reinforcement distributions fabricated by reaction hot pressing *J. Alloys Compd.* 581 (2013) 16–22
- [9]. S. Hao, J. Xie, Tensile properties and strengthening mechanisms of SiCp- reinforced aluminum matrix composites as a function of relative particle size ratio *J. Mater. Res.* 28 (2013) 2047– 55
- [10]. K.K. Alaneme, I.B. Akintunde, P.A. Olubambi, T.M. Adewale, Fabrication characteristics and mechanical behaviour of rice husk ash - Alumina reinforced Al-Mg-Si alloy matrix hybrid composites *J. Mater. Res. Technol.* 2 (2013) 60–67
- [11]. N. Barghout, A.B. Kashyout, M.A.M. Ibrahim, and Ahmed El Nemr, Novel Synthesis of SiC-SiO₂ Nanotubes from *Cinachyrella* sp. and Its Improvement of the Corrosion Resistance of Low Carbon Steel in 3.5% NaCl Water Solution, *Journal of Materials Engineering and Performance*, 16 (2023) 10857–10876
- [12]. G. Fadel, L.Z. Mohamed, G.A. Gaber, O. El kady, A. Elhabak, M. Adly, S.A. Abolkassem, Evaluation of corrosion and wear features of Al matrix reinforced with particles (SiC+Y₂O₃) coated with either nano-Ag/Ni or nano-Ag/Cu, *Egypt. J. Chem*, 67(8) (2024) 137–155.
- [13]. T. Lampke, A. Leopold, D. Dietrich, G. Alisch, B. Wielage, Correlation between structure and corrosion behaviour of nickel dispersion coatings containing ceramic particles of different sizes. *Surf Coat Technol* 201:3510–3517, 2006.
- [14]. B.E. Rani, J.B.B. Bai, Green Inhibitors for Corrosion Protection of Metals and Alloys: An Overview. *Int. J. Corros.* 2012, 2012, 380217.
- [15]. A. Zakeri, E. Bahmani, A.S.R. Aghdam, Plant Extracts as Sustainable and Green Corrosion Inhibitors for Protection of Ferrous Metals in Corrosive Media: A Mini Review. *Corros. Commun.* 2022, 1, 6–17.
- [16]. D.S. Chauhan, M.A. Quraishi, A.A. Sorour, C. Verma, A Review on Corrosion Inhibitors for High-Pressure Supercritical CO₂ Environment: Challenges and Opportunities. *J. Pet. Sci. Eng.* 2022, 215, 110695.
- [17]. M. Werle, Natural and Synthetic Polymers as Inhibitors of Drug Efflux Pumps. *Pharm. Res.* 2008, 25, 500–511.
- [18]. M. Finšgar, J. Jackson, Application of Corrosion Inhibitors for Steels in Acidic Media for the Oil and Gas Industry: A Review. *Corros. Sci.* 2014, 86, 17–41.
- [19]. A.A. Al-Amiery, W.N.R.W. Isahak, W.K. Al-Azzawi, Corrosion Inhibitors: Natural and Synthetic Organic Inhibitors, *Lubricants* 2023, 11, 174
- [20]. M.A.R. Khan, M.A. Habib, J. Naime, M.M.H. Rumon, M.S. Al Mamun, A.B.M. Nazmul Islam, M. Mahiuddin, K.M.R. Karim, M.H. Ara, A review on synthesis, characterizations, and applications of Schiff base functionalized nanoparticles, *Results in Chemistry* 6 (2023) 101160.
- [21]. R.H. Taha, G.A. Gaber, L.Z. Mohamed, W.A. Ghanem, Corrosion inhibition of two schiff base complexes on the mild steel in 1M HCl solution, *Egyptian Journal of Chemistry*, 62, Special Issue (Part 1) Innovation in Chemistry, 367–381.
- [22]. M. Mahdavian, M.M. Attar, Electrochemical behaviour of some transition metal acetylacetonate complexes as corrosion inhibitors for mild steel, *Corros. Sci.* 51 (2009) 409–414.
- [23]. K. Benbouguerra, S. Chafaa, N. Chafai, M. Mehri, O. Moumeni, A. Hellal, Synthesis, spectroscopic characterization and a comparative study of the corrosion inhibitive efficiency of an α -aminophosphonate and Schiff base derivatives: Experimental and theoretical investigations, *J. Mol. Struct.* 1157 (2018) 165–176,
- [24]. D. Daoud, T. Douadi, H. Hamani, S. Chafaa, M. Al-Noaimi, Corrosion inhibition of mild steel by two new S-heterocyclic compounds in 1 M HCl: Experimental and computational study, *Corros. Sci.* 94 (2015) 21–37.
- [25]. T. Lemaoui, N.E.H. Hammoudi, I.M. Alnashef, M. Balsamo, A. Erto, B. Ernst, Y. Benguerba, Quantitative structure properties relationship for deep eutectic solvents using Sr-profile as molecular descriptors, *J. Mol. Liq.* 309 (2020),
- [26]. D. Wang, S. Li, Y. Ying, M. Wang, H. Xiao, Z. Chen, Theoretical and experimental studies of structure and inhibition efficiency of imidazole derivatives, *Corros. Sci.* 41 (1999) 1911–1919.
- [27]. C. Öğretir, B. Mihçi, G. Bereket, Quantum chemical studies of some pyridine derivatives as corrosion inhibitors, *J. Mol. Struct. THEOCHEM.* 488 (1999) 223–231.
- [28]. C. Boulechfar, H. Ferkous, A. Delimi, M. Berredjem, A. Kahlouche, A. Madaci, S. Djellali, S. Boufas, A. Djedouani, A. Errachid, A.A. Khan, A. Boublia, T. Lemaoui, Y. Benguerba, Corrosion inhibition of Schiff base and their metal complexes with [Mn (II), Co (II) and Zn (II)]: Experimental and quantum chemical studies, *Journal of Molecular Liquids* 378 (2023) 121637.
- [29]. R.G. Parr, L.v. Szentpály, S. Liu, Electrophilicity Index, *J. Am. Chem. Soc.* 121 (1999) 1922–1924.
- [30]. S. Boudjelida, S. Djellali, H. Ferkous, Y. Benguerba, I. Chikouche, M. Carraro, Physicochemical Properties and Atomic-Scale Interactions in Polyaniline (Emeraldine Base)/Starch Bio-Based Composites: Experimental and Computational Investigations, *Polymers (Basel)*. 14 (2022) 1505.
- [31]. H. Ferkous, K. Rouibah, N.-E.-H. Hammoudi, M. Alam, C. Djilani, A. Delimi, O. Laraba, K.K. Yadav, H.-J. Ahn, B.-H. Jeon, Y. Benguerba, The Removal of a Textile Dye from an Aqueous Solution Using a Biocomposite Adsorbent, *Polymers (Basel)*. 14 (2022) 2396.
- [32]. H. Behloul, H. Ferkous, N. Bougdah, S. Djellali, M. Alam, C. Djilani, A. Sedik, D. Lerari, B.-H. Jeon, Y. Benguerba, New insights on the adsorption of CI-Reactive Red 141 dye using activated carbon prepared from the ZnCl₂-treated waste cotton fibers: Statistical physics, DFT, COSMO-RS, and AIM studies, *J. Mol. Liq.* 364 (2022).

- [33]. E. Ech-chihbi, M.E. Belghiti, R. Salim, H. Oudda, M. Taleb, N. Benchat, B. Hammouti, F. El-Hajjaji, Experimental and computational studies on the inhibition performance of the organic compound “2-phenylimidazo [1,2-a] pyrimidine-3-carbaldehyde” against the corrosion of carbon steel in 1.0 M HCl solution, *Surfaces and Interfaces*. 9 (2017) 206–217.
- [34]. M. Abdallah, H.M. Altass, A.S. Al-Gorair, J.H. Al-Fahemi, B.A.A.L. Jahdaly, K.A. Soliman, Natural nutmeg oil as a green corrosion inhibitor for carbon steel in 1.0 M HCl solution: Chemical, electrochemical, and computational methods, *J. Mol. Liq.* 323 (2021).
- [35]. F. El-Hajjaji, I. Merimi, M. Messali, R.J. Obaid, R. Salim, M. Taleb, B. Hammouti, Experimental and quantum studies of newly synthesized pyridazinium derivatives on mild steel in hydrochloric acid medium, *Mater. Today Proc.* 13 (2019) 822–831.
- [36]. A. Fathy, O. Elkady, A. Abu-Oqail, Synthesis and characterization of CueZrO₂ nanocomposite produced by thermochemical process. *J. Alloy Compd.* 719 (2017) 411–419.
- [37]. O. A. Elkady, S.A. Abolkassem, A.H. Elsayed, W.A. Hussein, K.F.A. Hussein, Microwave absorbing efficiency of Al matrix composite reinforced with nano-Ni/SiC particles, *Results in Physics* 12, (2019), 687–700.
- [38]. B. Ryang Kim, K. DoWoo, J. Kook Yoon, Jung-Mann Doh, In-Jin Shon “Mechanical properties and rapid consolidation of binderless niobium carbide” *Journal of Alloys and Compounds*, V. 481 (2009) 573–576.
- [39]. S. Hosny, G.A. Gouda, S.M. Abu-El-Wafa, Novel nano copper complexes of a new Schiff base: green synthesis, a new series of solid Cr (II), Co (II), Cu (II), Pd (II) and Cd (II) chelates, characterization, DFT, DNA, antitumor and molecular docking studies. *Applied Organometallic Chemistry* 2022, 36(5):6627.
- [40]. S. Hosny, R.F.A. El-Baki, Z.H.A. El-Wahab, G.A. Gouda, M.S. Saddik, A. Aljuhani, A.M. Abu-Dief, Development of novel nano-sized imine complexes using Coriandrum sativum extract: structural elucidation, non-isothermal kinetic study, theoretical investigation and pharmaceutical applications. *International Journal of Molecular Sciences* 2023, 24(18):14259.
- [41]. S. Hosny, M.S. Ragab, R.F. Abd El-Baki. Synthesis of a new sulfadimidine Schiff base and their nano complexes as potential anti-COVID-19 and anti-cancer activity. *Scientific Reports* 2023, 13(1):1502.
- [42]. G.A. Gaber, L.Z. Mohamed, G. Hamdy, Enhancing Corrosion Behavior of T91 Steel in 3.5% NaCl through Graphene Oxide Nanocomposite Coatings, *Egypt. J. Chem.* 68 (2025).
- [43]. G.A. Gaber, H.A. Aly, K.A. Abdelghafar, L.Z. Mohamed, Optimizing the Corrosion Parameters and Assessing Corrosion Inhibitions for Cast Cu45Mn25Al15Fe5Cr5Ni5 HEA in Nitric Acid Solution via DOE and RSM Analysis, *Indian Journal of Pure and Applied Physics*, 62, 897-910.
- [44]. G.A. Gaber, L.Z. Mohamed, H.A. Aly, S. Hosny, Corrosion potential and theoretical studies of fabricated Schiff base for carbidic austempered ductile iron in 1M H₂SO₄ solution, *BMC chemistry*, 18, 170 (2024).
- [45]. I. Azcona, A. Ordóñez, J.M. Sánchez, F. Castro, Hot isostatic pressing of ultra fine tungsten carbide-cobalt hard metals. *J Mater Sci*, 37 (2002) 4189–95.
- [46]. S. Abolkassem, A. Elsayed, S. Kariya, J. Umeda, K. Kondoh, Influence of thermo-mechanical processing on microstructure and properties of bulk metallic glassy alloys-reinforced Al matrix composites prepared by powder metallurgy, *Journal of Materials Research and Technology*, 27, (2023), 8197-8208.
- [47]. V. Bonache, M.D. Salvador, A. Fernández, A. Borrell *Int. Journal of Refractory Metals and Hard Materials* 29 (2011) 202–208.
- [48]. S.S. Razavi-Tousi, R. Yazdani-Rad, S.A. Manafi, Effect of volume fraction and particle size of alumina reinforcement on compaction and densification behavior of Al–Al₂O₃ nanocomposites, *Mater. Sci. Eng. A* 528 (2011) 1105–1110.
- [49]. A. Canakci, T. Varol, Microstructure and properties of AA 7075/Al–SiC composites fabricated using powder metallurgy and hot pressing. *powder technology*, 268(2014), 72-79.
- [50]. M. Yang, D. Zhang, X. Gu, L. Zhang, Effect of SiC particle size on CTEs of SiC /Al composites by pulsed electric current sintering, *materials chemistry and physics* 99(2006)170-173.
- [51]. V. Bonache, M.D. Salvador, A. Fernández, A. Borrell *Int. Journal of Refractory Metals and Hard Materials* 29(2011) 202–208.
- [52]. O. Elkady, A. Fathy, Effect of SiC particle size on the physical and mechanical properties of extruded Al matrix composite nano composites, *material and design*, 54, (2014), 348-353.
- [53]. H. M. YEHYA, W. M. Daoush, M. H. El-Sayed, A. E. El-Nikhaily, 3rd International Conference in Africa and Asia on Welding and Failure Analysis of Engineering Materials, 2015, Luxor, Egypt.
- [54]. Y.L. Dong, F.M. Xu, X.L. Shi, C. Zhang, Z.J. Zhang, J.M. Yang, Y. Tan, Fabrication and mechanical properties of nano-/micro-sized Al₂O₃/SiC composites, *Mater. Sci. Eng. A* 504 (2009) 49–54.
- [55]. A. Canakci, Microstructure and abrasive wear behaviour of B₄C particle reinforced 2014 Al matrix composites, *Mater. Sci.* 46 (2014) 2805–2813.
- [56]. W. Klaus, richter, H. Ipsen. the Al-Ni- Si phase diagram between 0 and 33.3 at.%Ni Intermetallics, 11(2003), 101-109.
- [57]. K. Liu, Y. Li, J. Wang, In situ reactive fabrication and effect of phosphorus on microstructure evolution of Ni/Ni-Al intermetallic composite coating by laser cladding, *Mater. Design*, 105(2016)171-178.
- [58]. F. Kretz, Z. Gacs, J. Kovacs, T. Piezonka, the electroless deposition of nickel on SiC particles for aluminum matrix composites *Surface and Coatings Technology* 180 – 181 (2004) 575–579.
- [59]. H.M. Zakaria, microstructure and corrosion behavior of Al/SiC metal matrix composites, *Ain shams engineering journal*, 5(2014)831-839.
- [60]. F. Kertz, Z. Gacs, J. Kovacs, T. Piezonka, the electroless deposition of nickel on SiC particles for Al matrix composites, *surface and coating technology* 180- 181(2004)574-579.

- [61]. F. Teng, K. Yu, J. Luo, H. Fang, C. Shi, Y. Dai, H. Xiong, Microstructure and properties of Al- 50%SiC composites for electronic packaging applications, *Trans. Nonferrous Met. Soc. China* 26(2016)2647-2652.
- [62]. S. Abolkasem, O. Elkady, A. Elsayed, W. Hussein, H. Yehia, Effect of consolidation techniques on the properties of Al matrix composite reinforced with nano Ni-coated SiC, results in physics, 9(2018) 1102-1111.
- [63]. H. Yu, Q. Dong, Y. Chen, C. Chen, Influence of silicon on growth mechanism of microarc oxidation coating on cast Al-Si alloy R. Soc. Open Sci. 5 (2018) 1069-72
- [64]. J. Datta, S. Datta, M.K. Banerjee, S. Bandyopadhyay, Beneficial effect of scandium addition on the corrosion behavior of Al-Si-Mg-SiCp metal matrix composites *Compos. Part A Appl. Sci. Manuf.* 35 (2004) 1003-8
- [65]. A. Pardo, M.C. Merino, S. Merino, F. Viejo, M. Carboneras, R. Arrabal, Influence of reinforcement proportion and matrix composition on pitting corrosion behaviour of cast aluminium matrix composites (A3xx.x/SiCp) *Corros. Sci.* 47 (2005) 1750-64
- [66]. P.P. Trzaskoma, Corrosion Behavior of SiC/Al Metal Matrix Composites *J. Electrochem. Soc.* 130 (1983) 1804
- [67]. D.M. Aylor, P.J. Moran, Effect of Reinforcement on the Pitting Behavior of Aluminum-Base Metal Matrix Composites. *Proc. - Electrochem. Soc.* 84-9 (1984) 584-95
- [68]. Y. Shimizu, T. Nishimura, I Matsushima, Corrosion resistance of Al-based metal matrix composites *Mater. Sci. Eng. A* 198 (1995) 113-8
- [69]. A.J. Trowsdale, B. Noble, S.J. Harris, H.S.R. Gibbins, G.E. Thompson, G.C. Wood, The influence of silicon carbide reinforcement on the pitting behaviour of aluminium *Corros. Sci.* 38 (1996) 177-91
- [70]. C. Monticelli, F. Zucchi, G. Brunoro, G. Trabaneli, Stress corrosion cracking behaviour of some aluminium-based metal matrix composites *Corros. Sci.* 39 (1997) 1949-63
- [71]. Z. Feng, C. Lin, J. Lin, J. Luo, Pitting behavior of SiCp/2024 Al metal matrix composites *J. Mater. Sci.* 33 (1998) 5637-5642
- [72]. K. Alaneme, Corrosion Behaviour of Heat-Treated Al-6063/SiCp Composites Immersed in 5 wt % NaCl Solution *Leonardo J. Sci.* (2011) 55-64
- [73]. H.M. Zakaria, Microstructural and corrosion behavior of Al/SiC metal matrix composites *Ain Shams Eng. J.* 5 (2014) 831-8
- [74]. A.K. Mishra, R. Balasubramaniam, Corrosion inhibition of aluminum alloy AA 2014 by rare earth chlorides *Corros. Sci.* 49 (2007) 1027-44
- [75]. C. He, D. Lou, J. Wang, Q. Cai, Corrosion protection and formation mechanism of anodic coating on SiC p/Al metal matrix composite *Thin Solid Films* 519 (2011) 4759-4764
- [76]. W. Xue, X. Wu, X. Li, H. Tian, Anti-corrosion film on 2024/SiC aluminum matrix composite fabricated by microarc oxidation in silicate electrolyte *J. Alloys Compd.* 425 (2006) 302-306.
- [77]. S. Erdoğan, B. Tüzün, Relationship Between the Chemical Structure and the Corrosion Inhibition Properties of Some Organic Molecules: Challenges and Industrial Applications. In: *Handbook of Research on Corrosion Sciences and Engineering*. IGI Global; 2023: 42-64.
- [78]. S. Hosny, A. Abdelfatah, G.A. Gaber, Synthesis, characterization, synergistic inhibition, and biological evaluation of novel Schiff base on 304 stainless steel in acid solution. *Scientific Reports* 2024, 14(1):470.
- [79]. S.K. Saha, P. Banerjee, Inhibition of metallic corrosion by N, O, S donor Schiff base molecules. In: *Conceptual Density Functional Theory and Its Application in the Chemical Domain*. CRC Press; 2018: 145-194.
- [80]. H.M. Al-Saidi, G.A. Gouda, M. Abdel-Hakim, N.I. Alsenani, A. Alfarsi, M.H. Mahross, O. Farghaly, S. Hosny, Synthesis and characterization of Ni (II), Cu (II), Zn (II) and Azo dye based on 1, 10-o-phenanthroline binary complexes: Corrosion inhibition properties and computational studies. *International Journal of Electrochemical Science* 2022, 17(3):220333.
- [81]. G.A. Gaber, S. Hosny, L.Z. Mohamed, Experimental and theoretical studies of 2-cyano-N-(4-morpholinobenzylidene) acetohydrazide as corrosion inhibitor for galvanized steel and 304 stainless steel in 1M H₂SO₄ solution. *International Journal of Electrochemical Science* 2021, 16(12):211214.
- [82]. R. Singh, A. Kumar, R. Tiwari, P. Rawat, V. Gupta, A combined experimental and quantum chemical (DFT and AIM) study on molecular structure, spectroscopic properties, NBO and multiple interaction analysis in a novel ethyl 4-[2-(carbamoyl) hydrazinylidene]-3, 5-dimethyl-1H-pyrrole-2-carboxylate and its dimer. *Journal of Molecular Structure* 2013, 1035:427-440.